

Abstract

Large-eddy simulations of a turbulent boundary layer with $Re_{\delta^*} = 3500$ were performed with two grid resolutions. The computations were continued for sufficient time to obtain frequency spectra with resolved frequencies that correspond to the most important structural frequencies on an aircraft fuselage. The turbulent stresses were adequately resolved with both resolutions. Detailed quantitative analysis of a variety of statistical quantities associated with the wall-pressure fluctuations revealed similar behavior for both simulations. The primary differences were associated with the lack of resolution of the high-frequency data in the coarse-grid calculation and the increased jitter (due to the lack of multiple realizations for averaging purposes) in the fine-grid calculation. A new curve fit was introduced to represent the spanwise coherence of the cross-spectral density.

1 Introduction

Reduced levels of aircraft interior cabin noise are desirable for both comfort and health-related reasons. Blake [1] notes that a turbulent boundary layer on the fuselage at locations forward of the engines dominates the excitation of the fuselage structure. Boeing 737 flight experiments by Wilby and Gloyna [2] confirm the contributions of turbulent boundary-layer pressure fluctuations to the noise level inside the aircraft cabin. Clever use of fuselage materials and arrangement of the frames and stringers provides some opportunity for reducing the amount of vibration transmitted to the interior cabin. However, to design such a structure, detailed information with regard to wall-pressure fluctuations in the external turbulent boundary layer is required.

The finite size of physical transducers accounts for much of the difficulty in obtaining the desired measurements. Because the pressure field is convected with the flow, a lack of resolution in space also limits the effective temporal resolution of the signal. The speed at which a pressure disturbance convects downstream is characterized by the convection velocity U_c , which tends to be a weak function of both the frequency of the pressure signal f and the streamwise separation distance ξ . The important link between the time and space resolutions of the pressure has been long appreciated. Corcos [3] proposed a correction to the pressure statistics based on a model of the pressure field in which the coherence function of the cross-spectral density was dependent upon similarity variables. Further support for his model of the wall-pressure field was presented in Ref. [4]. Also in Ref. [4], Corcos argued that terms that are quadratic in the turbulent-fluctuation velocities are largely responsible for the wall-pressure fluctuations. A direct numerical simulation (DNS) of turbulent channel flow by Kim [5] confirmed the importance of the nonlinear source terms.

Using the same database as Kim [5], Choi and Moin [6] carefully analyzed various correlations of the wall-pressure fluctuations. They showed that the low-frequency data was most appropriately scaled with outer flow variables and that the high-frequency data scaled best with the wall-layer or inner flow, variables. Only at high wavenumbers and frequencies did they observe Corcos's proposed similarity of the cross-spectral density. In addition, Choi and Moin [6] calculated convection velocities as functions of frequency, wavenumber, and separation distance. Large structures convected with a more uniform velocity than did smaller structures.

Extensive measurements by Schewe [7] with five different sizes of pressure transducers suggest the validity of the Corcos correction for $\omega d/U_c < 8$, where $\omega = 2\pi f$ and d is the diameter of the pressure transducer. Schewe found that the Corcos-corrected values of the root-mean-square (rms) wall pressure were obtained with probes that have diameters as large as approximately

160 viscous wall units. For larger probes, he found that the correction suggested by Corcos was too small. However, Schewe points out that the lack of success of the correction for very large probes could be associated with the data that Corcos used and not the form of the model *per se*.

Flight tests by Efimtsov [8] at a variety of Mach numbers (all with zero pressure gradient), support the general form of the Corcos [3, 4] approximations, although the details of the streamwise and spanwise coherence functions need to be determined for three separate frequency ranges.

Farabee and Casarella [9] performed an extensive set of measurements that provide insight into the spectral features of turbulent wall-pressure fluctuations. Although the measurements were made at relatively low Reynolds numbers, their use of multiple flow velocities produced a Reynolds-number range of nearly a factor of 2 in the same facility. Their measurements clearly identified three spectral regions. A low-frequency regime displayed ω^2 behavior. A mid-frequency range indicated that the spectral density data for all Reynolds numbers tested collapsed to a single curve when nondimensionalized with the friction velocity, the wall shear stress, and the boundary-layer thickness. In the high-frequency range, inner wall variable scalings collapse the data at all Reynolds numbers onto a single curve. Plots of the coherence function of the frequency–streamwise-separation cross-spectral density versus the phase of the cross-spectral density showed similarity at high frequencies, as would be expected from the Corcos model [3, 4]. However, a low-frequency cutoff also existed; significant deviations from the similarity curve were observed below the cutoff frequency. The variations of the convection velocity with both frequency and separation distance were investigated. Quantitative differences in the convection velocity with the results of the channel-flow calculations of Choi and Moin [6] were attributed to the unique features of channel flows. In particular, Farabee and Casarella [9] contended that the low-frequency data are particularly sensitive to turbulent structures in the outer portion of the boundary layer and that these structures are significantly different between boundary layers and channel flows.

A set of turbulent-channel-flow large-eddy-simulation (LES) calculations performed by Chang, Abraham, and Piomelli [10] suggests the feasibility of obtaining useful wall-pressure fluctuation data in the context of an LES calculation. In spite of the use of a model for the small scales of motion, plots of the spectral density and contours of the frequency–streamwise-wavenumber spectra were quite similar to results obtained with DNS, especially for the lower frequencies.

The current work involves an LES of a zero-pressure-gradient boundary layer with a turbulent Reynolds number that is five times greater than that used in the previous calculations of space-time wall-pressure statistics. The major objective of this work is to obtain statistics of the wall-pressure fluctuations in a frequency range that is relevant to the dominant structural vibration modes of an aircraft fuselage.

2 Mathematical Considerations

2.1 The Large-Eddy Simulation

LES is used to compute the large scales of fluid motion (i.e., the resolved scales) in the boundary layer; the small scales of motion (i.e., the subgrid scales (SGS)) are modeled. A filtering operation

distinguishes between the resolved scales and the SGS such that

$$\bar{q}(\mathbf{x}) = \int_D q(\mathbf{x}') G(\mathbf{x}, \mathbf{x}') d\mathbf{x}' \quad (1)$$

where q represents a flow quantity, \mathbf{x} is the position vector, D represents the domain of the flow, G is the filtering function, and \mathbf{x}' is a dummy variable of integration. The overbar designates a filtered (resolved) quantity. The incompressible Navier-Stokes equations are made nondimensional, with the displacement thickness δ^* as the length scale and the free-stream velocity U_0 as the velocity scale. The pressure p has been normalized with ρU_0^2 , where ρ is the density; the displacement-thickness Reynolds number Re_{δ^*} is $U_0 \delta^* / \nu$, where ν is the kinematic viscosity. In Cartesian coordinates, the velocity in a general coordinate direction x_i is u_i . With the use of the Einstein summation convention, the filtered continuity equation is

$$\frac{\partial \bar{u}_i}{\partial x_i} \quad (2)$$

and the filtered momentum equations are

$$\frac{\partial \bar{u}_i}{\partial t} + \frac{\partial(\bar{u}_i \bar{u}_j)}{\partial x_j} = -\frac{\partial \bar{p}}{\partial x_i} - \frac{\partial \tau_{ij}}{\partial x_j} + \frac{1}{Re_{\delta^*}} \frac{\partial^2 \bar{u}_i}{\partial x_j \partial x_j} \quad (3)$$

where the SGS stress tensor is defined as

$$\tau_{ij} \equiv \overline{u_i u_j} - \bar{u}_i \bar{u}_j \quad (4)$$

No-slip and impermeability conditions are imposed at the wall; the disturbances decay asymptotically in the far field. The Lilly [11] formulation of the dynamic SGS model of Germano, Piomelli, Moin, and Cabot [12] was used in conjunction with a Fourier cutoff filter in the streamwise and spanwise directions. The model test filter was twice as large as the grid filter. No filtering was performed in the wall-normal direction. The implementation of the model involved the redefinition of the pressure variable to include the trace of the SGS stress tensor τ_{kk} . Because τ_{kk} vanishes at the wall, the wall pressure retains its original meaning.

The need for a lengthy time series to obtain adequate frequency resolution mandates the very efficient solution of the flow equations. A Fourier-Chebyshev pseudospectral collocation scheme is used to spatially discretize the skew-symmetric form of Eqs. (2) and (3). A semi-implicit numerical time-advancement scheme, in combination with the fractional time-step method described in Zang and Hussaini [13], integrates the system forward in time. Chang, Abraham, and Piomelli [10] indicate the importance of dealiasing in the Fourier directions for these calculations; hence, this practice is continued here. However, unless otherwise specified, grid sizes mentioned later refer to the full grid used for the computation of the nonlinear terms. The use of Fourier expansions in the streamwise direction obviates the need for prescribed inflow conditions; however, because turbulent boundary layers are not parallel and homogeneous, the implied periodicity of the Fourier expansions necessitates special treatment of the equations. In this work, the additional treatment involves casting the equations in non-Cartesian ‘‘similarity’’ coordinates, as described in detail by Spalart and Leonard [14] and Spalart [15]. This approach is summarized below.

2.2 Similarity Coordinates

A Cartesian coordinate system in which x , y , and z represent the streamwise, spanwise, and wall-normal directions is modified, first by the introduction of a new coordinate ζ , which replaces z as the wall-normal variable. Near the wall, lines of constant ζ are approximately parallel to the wall and correspond to lines of constant wall-normal coordinate z . Away from the wall region, lines of constant ζ are approximately parallel to the turbulent boundary-layer edge. The slope of the constant ζ lines with respect to the wall is denoted by S . The formal transformation of the Cartesian coordinates to the non-Cartesian system with an associated change of dependent variables, such that the form of the transport terms in the Navier-Stokes equations remains unchanged, is discussed in detail by Spalart [15].

The resulting set of equations is further modified by noting that the boundary-layer thickness, the mean-flow profiles, and the turbulent statistics vary slowly with downstream location. We can isolate this slow dependence by decomposition of the streamwise velocity U as

$$U(x, y, \zeta, t) = U_m(x, \zeta) + A(x, \zeta)u(x, y, \zeta, t) \quad (5)$$

where U_m is the mean-velocity profile at location x and A is an ‘‘amplitude function’’ that is proportional to the rms of the fluctuations. The quantity u has zero mean and its rms value is independent of streamwise location; hence, the imposition of streamwise periodicity, although not fully justified, does not flagrantly violate the physics. Differentiation of Eq. (5) with respect to the streamwise direction provides

$$\frac{\partial U}{\partial x} = \frac{\partial U_m}{\partial x} + A \frac{\partial u}{\partial x} + u \frac{\partial A}{\partial x} \quad (6)$$

The slow variation of the basic flow properties can be modeled by a dependence on a ‘‘slow’’ streamwise coordinate X . On the other hand, the turbulent motions involve fluctuations on much smaller scales. The ‘‘fast’’ streamwise coordinate on which the turbulent motions vary retains the designation x . Hence, with respect to Eq. (6), the streamwise variations of U_m and A are slow and can be written as $\partial U_m / \partial X$ and $\partial A / \partial X$, respectively; the variation of u occurs on the fast scale. Similar decompositions are made for the other flow components. The quantity A scales with the friction velocity $u_\tau \equiv \sqrt{\tau_w / \rho}$ (where τ_w is the wall shear stress), and this quantity goes to 0 as the Reynolds number tends to infinity. Appropriate scaling of all quantities and retention of terms up to $O((u_\tau / U_0)^2)$ produces a modified set of equations with additional unknown quantities that involve the coordinate-line slope S and derivatives of statistical quantities with respect to the slow scale X . The modifications to the equations are easily incorporated into the basic solution scheme once the new unknown quantities are determined.

To specify these unknown quantities, a reference calculation is performed where standard high-Reynolds-number turbulence correlations and the integral momentum equation are used to find values for the unknown quantities. The appropriate correlations are discussed by Spalart and Leonard [14]. The results of the reference calculation provide the necessary turbulent statistical quantities at a single upstream position X_0 . These quantities are then used to perform a backwards difference differentiation to obtain the X derivatives in the current calculation. This procedure is described by Spalart [15].

The use of the similarity coordinates permits the calculation to be performed in a streamwise periodic domain that resolves the turbulent fluctuations on the fast scale x but has the

constant turbulent statistical quantities associated with location X . The calculation is useful for the determination of the desired statistical quantities and any flow physics that occur on the turbulent length scale.

2.3 Scalings

The time sample for the calculation was chosen to capture frequencies that would be relevant for the important structural vibration modes of an aircraft fuselage in flight. The targeted frequency range was between 100 and 2000 Hz. Previous works [6, 9, 10] indicate that the appropriate nondimensional frequency variable that collapses low-frequency data over a large Reynolds-number range is proportional to the product of frequency and a boundary-layer thickness divided by the friction velocity. The displacement thickness δ^* will be used as the boundary-layer thickness. To obtain appropriate flight values of δ^* and u_τ , reference flight conditions were chosen from the Boeing 737 experiments of Wilby and Gloyna [2]. The free-stream speed U_0 was 241 m/s and the displacement thickness of the turbulent boundary layer was about 1.2 cm. At the flight altitude, these conditions correspond to a boundary layer with a Reynolds number $Re_\delta^* = 105350$. For the reference conditions, the turbulent flow correlation Eq. (21.5) of Schlichting [16] gives $u_\tau/U_0 = 0.027$. Hence, the corresponding target frequency range of the simulations is $1.16 \leq \omega\delta^*/u_\tau \leq 23.17$. The length of the time sample required in the simulation is easily obtained after δ^* and u_τ have been determined at the Reynolds number of the simulation.

2.4 Flow Parameters

The calculations are performed for an incompressible flat-plate boundary layer with a Reynolds number $Re_\delta^* = 3500$. The turbulent Reynolds number $Re_t = u_\tau\delta/\nu$ is approximately 1000 when δ is chosen as the distance from the wall at which the the mean streamwise velocity is $0.99U_0$. The reference flow that is used for backwards differencing is computed at $Re_\delta^* = 2200$. The streamwise and spanwise domain lengths are $L_x/\delta^* = 44.88$ and $L_y/\delta^* = 14.28$, respectively. In terms of viscous length scales, $L_x u_\tau/\nu = 6409$ and $L_y u_\tau/\nu = 2040$. Two-point streamwise velocity correlations in the near-wall region decay to a few percent for correlation distances of $L_x/2$; hence, the streamwise domain is sufficiently long for a turbulence simulation. Several wall-layer streaks exist across the span. The spanwise length is determined by the need for a sufficient decay in the spanwise wall-pressure correlation.

2.5 Statistics

The statistical quantities that will be presented include the wall-pressure mean square, skewness, and flatness; the spatial coherence of the wall pressure correlations in both the streamwise and spanwise directions; the one-dimensional (1-D) temporal spectrum; the two-dimensional (2-D) temporal–streamwise-wavenumber spectrum; the coherence functions of the cross-spectral density with streamwise and spanwise separations; and the convection velocity. These quantities are described below.

The wall-pressure mean square, skewness, and flatness will all be similarly computed. The mean square is

$$MS = \langle p^2 \rangle \quad (7)$$

where p is the wall pressure and the angle brackets $\langle \rangle$ imply an average over an appropriate sample. In addition to averaging over the time domain, because the streamwise and spanwise directions are homogeneous, the average is also performed over both directions. The mean square and the corresponding rms provide information with respect to the intensity of the pressure fluctuations. The skewness is defined as

$$\frac{\langle p^3 \rangle}{\langle p^2 \rangle^{3/2}} \quad (8)$$

and is a measure of the polarity of high-amplitude events. A Gaussian distribution of the wall pressure results in a skewness of 0. The flatness is a measure of the importance of infrequent high-amplitude events and is defined as

$$\frac{\langle p^4 \rangle}{\langle p^2 \rangle^2} \quad (9)$$

A Gaussian distribution has a flatness of 3. As the size of the averaging area of a pressure transducer increases, the skewness and flatness approach their Gaussian limits [7].

The spatial correlations are most usefully defined in terms of their coherence function

$$R(\xi, \eta) = \frac{\langle p(x, y)p(x + \xi, y + \eta) \rangle}{\langle p^2 \rangle} \quad (10)$$

where x and y are arbitrary streamwise and spanwise coordinates in the computational domain and ξ and η are the streamwise and spanwise separation distances. The spatial periodicity of the flow restricts meaningful correlation distances to half of the streamwise and spanwise domain. The correlations with separation distances in excess of the half-lengths are reflections of the correlations with smaller separation distances.

The optimal sampling of temporal spectra requires the partition of the time-series data. The total time sample of the computation is subdivided into 12 nonoverlapping subsections; each subsection has a period $1/2T$ such that $(1/2T)u_\tau/\delta^* = 2.81$. This period corresponds to a minimum frequency $\omega\delta^*/u_\tau = 2.24$, which is slightly less than twice the minimum target frequency. The 12 subsections are then linked to form 11 ensemble units such that the first unit consists of the first and second subsections, the second unit consists of the second and third subsections, and so on. Each ensemble unit contains a sequential time history with a period $Tu_\tau/\delta^* = 5.62$ and a minimum frequency resolution $\omega\delta^*/u_\tau = 1.12$. The use of overlapping ensemble units as described above is optimal, or very nearly so, in the sense that the smallest spectral variance per data point is realized [17]. The variance of the spectral estimates are reduced by the product of the fraction 9/11 and the number of averaging samples [17].

The spectra are determined with the use of Fourier transforms of the windowed wall-pressure data; hence,

$$\Phi(\omega, k_x) = C \left\langle \left| \frac{1}{(2\pi)^2} \int_0^T \int_0^{L_x} d(t)p(x, y, t) \exp(-i\omega t) \exp(-ik_x x) dx dt \right|^2 \right\rangle \quad (11)$$

where $i = \sqrt{-1}$, T is the time period, L_x is the domain length in the streamwise direction, k_x is the streamwise wavenumber, d is the windowing function for the time series, and C is the

analytic correction factor for the windowing function as given by Hardin [18]:

$$C = \frac{2\pi}{\int_0^T d^2(t) dt} \quad (12)$$

For the 2-D spectrum, the angle brackets imply an average over the spanwise direction. The data window

$$d(t) = \frac{1}{2} \left[1 - \cos \left(\frac{t}{T} \right) \right] \quad (13)$$

is that of Hann, as given in Ref. [17]. The streamwise periodicity of the raw data makes the use of a data window in the x direction unnecessary. The use of an explicit, analytic correction factor to account for the data windowing permits the use of Parseval's theorem

$$\frac{1}{TL_x} \int_0^T \int_0^{L_x} p^2 dx dt = \int_{-\infty}^{\infty} \int_{-\infty}^{\infty} \Phi(k_x, \omega) dk_x d\omega \quad (14)$$

as an independent check of the validity of postprocessing computer codes. Parseval's theorem is typically satisfied to within a few percent. In practice (because $\Phi(k_x, \omega)$ is symmetric about $\omega = 0$), only $\omega \geq 0$ is considered, and the value of $\Phi(k_x, \omega)$ is doubled (except for $\omega = 0$) to preserve Parseval's equality. The 1-D temporal spectrum is easily computed by integration of the 2-D spectrum; that is,

$$\phi(\omega) = \int_{-\infty}^{\infty} \Phi(k_x, \omega) dk_x \quad (15)$$

The 1-D temporal spectrum can also be computed by calculating only the temporal Fourier transform and taking the streamwise and spanwise average. Plots of the results of these two methods of calculation are indistinguishable. The 2-D temporal–spanwise–wavenumber spectrum can also be computed in the same way as the 2-D temporal–streamwise–wavenumber spectrum by substituting y for x , k_y for k_x , and L_y for L_x in Eq. (11).

In the field of wall-pressure fluctuations, the function

$$, (\xi, \eta, \omega) = \left\langle \frac{C}{2\pi} \int_0^T d(t) p(x, y, t) p(x + \xi, y + \eta, t) \exp(-i\omega t) dt \right\rangle \quad (16)$$

is commonly called the cross-spectral density. The cross-spectral density function is typically computed by determining the full spatial-temporal spectrum and then applying inverse Fourier transforms in the spatial directions. Corcos [3, 4] suggested expressions for the cross-spectral density function $, (\xi, \eta, \omega)$ for cases in which $\xi = 0$ or $\eta = 0$. His expressions

$$, (\xi, 0, \omega) = \phi(\omega) A(\alpha) \exp(-i\alpha) \quad (17)$$

and

$$, (0, \eta, \omega) = \phi(\omega) B(\beta) \quad (18)$$

are in terms of the similarity variables

$$\alpha \equiv \omega \xi / U_c \quad (19)$$

and

$$\beta \equiv \omega\eta/U_c \quad (20)$$

Note that $\phi(\omega) = \langle \cdot, (0, 0, \omega) \rangle$. The functions A and B are the coherence functions of the cross-spectral densities. The convection velocity U_c can be thought of as the speed at which a pressure disturbance of fixed frequency travels downstream. This speed is formally determined by

$$\alpha = -\tan^{-1}(\cdot, i/\cdot, r) \quad (21)$$

where \cdot, r and \cdot, i are the real and imaginary parts of \cdot, \cdot , respectively. Hence, the similarity variable α corresponds to the phase of the cross-spectral density. In practice, the convection velocity is found to be a weak function of the separation distance ξ and the frequency ω . A variety of different approaches have been employed to estimate U_c . Independent of the value of U_c , the Corcos functions A and B are uniquely determined as

$$A = |\langle \cdot, (\xi, 0, \omega) \rangle| / \phi(\omega) \quad (22)$$

and

$$B = |\langle \cdot, (0, \eta, \omega) \rangle| / \phi(\omega) \quad (23)$$

Because of the homogeneity of the flow, no explicit dependence on the x and y locations needs to be recited.

2.6 Numerical Accuracy

The computer code used for these calculations is a variant of the code used in the numerical simulations of Zang and Hussaini [19]. The computations are spectrally accurate in the three spatial directions. A hybrid time-advancement algorithm uses the Crank-Nicolson scheme on the implicit portion and a third-order Runge-Kutta method for the explicit portion. Formally, the hybrid scheme is second-order accurate in time. A fixed time step was used to facilitate the use of fast Fourier transforms on the wall-pressure time series. To ensure that the maximum CFL number remained within the stability bounds of the third-order Runge-Kutta method, the time-step size was chosen so that the average CFL number was about 2/3 of the maximum allowable size.

In addition to the usual code-validation tests that simulate Tollmien-Schlichting waves, typical turbulence quantities have been evaluated and found to be consistent with previous researchers' results. The mean-flow profile and the rms turbulence intensities are shown in Fig. 1 and Fig. 2, respectively. The mean-flow profile contains a small log layer with the correct slope. The turbulence intensity profiles are similar to those plotted in Fig. 3 of Piomelli [20].

The calculations described herein were performed on a mesh of $96 \times 96 \times 64$ grid points in the streamwise, spanwise, and wall-normal directions, respectively. The use of an average value of $0.0408U_0$ for the friction velocity determines the grid spacings in terms of viscous length scales. Quantities normalized with the viscous scales u_τ and ν/u_τ are denoted by a superscript $+$. The streamwise and spanwise grid spacings are $\delta x^+ = \delta x(u_\tau/\nu) = 66.7$ and $\delta y^+ = \delta y(u_\tau/\nu) = 21.3$. Because dealiasing is used in these two directions, the actual minimum resolved scales in the streamwise and spanwise directions are 100.1 and 31.9, respectively. The grid point nearest the wall is at a location $z^+ = 0.34$. All grid spacings are well within the resolution guidelines for turbulent LES set forth by Piomelli [20].

The grid resolution was further checked by rerunning a portion of the calculation with greater grid resolution. The high-resolution sample was run on a $192 \times 128 \times 64$ grid. The time-averaged friction velocity is 0.0412, slightly higher than that which was calculated for the case of the coarser grid. For an optimally run LES, a change in the grid resolution changes the definition of what constitutes a large eddy. As the grid is refined, the SGS model accounts for less of the turbulent activity. Figures 3(a) and 3(b) show the decomposition of the primary shear stress components for the two different resolutions, respectively. Even in the coarse-grid case, the SGS stress never accounts for more than 10 percent of the total stress. In the finer grid case, the SGS model accounts for an even smaller portion of the stress. Increased resolution implies that more of the turbulent motions will be included in the resolved turbulence and less will be absorbed by the SGS model. This feature of LES implies that “grid independence” of an LES cannot be established by the use of pointwise comparisons of flow fields at different grid resolutions. The concept of grid independence of an LES can only be established in view of the objectives of the particular calculation. In the present study, the objectives are to obtain certain statistical correlations of the wall pressure. If these statistical quantities can be shown to be independent of the grid used, then for the purposes of this study, the calculation is sufficiently well resolved. Comparisons of the relevant statistics appear in section 3.

3 Results

3.1 Time-Averaged Quantities

The scalar statistics that characterize the global features of the wall-pressure fluctuations are tabulated in Table 1. These data are averaged over both the spatial dimensions and time. The low-resolution data are averaged over all 12 temporal subsections described above. The high-resolution data are averaged over only two equivalent temporal subsections. The rms and mean-square quantities are normalized with the time-averaged wall shear from the respective calculations. The rms is computed as the square root of the mean square. The \pm quantities for mean square, skewness, and flatness are the standard deviations in the time sample of the respective spatially averaged quantities.

Table 1: Time-Averaged Wall-Pressure Statistics

Simulation	p_{rms}/τ_w	MS/τ_w^2	Skewness	Flatness
High resolution	2.74	7.52 ± 0.34	-0.002 ± 0.082	4.74 ± 0.46
Low resolution	2.60	6.76 ± 0.71	0.036 ± 0.115	4.30 ± 0.51

The computed mean-square pressures are somewhat lower than the 8.54 value predicted by Eq.(2) of Farabee and Casarella [9]. The greater level of the mean-square pressure computed with the high-resolution LES suggests that the discrepancy could be a consequence of limited spatial (and, hence, temporal) resolution of the LES. This possibility will be discussed more fully below in relation to the spectra. Another possibility is that Eq.(2) of Ref. [9] overestimates the mean-square pressure. Close inspection of the rms pressures in Fig. 2 of Ref. [9] reveals that the data for $Re_t \leq 1000$ generally lies below the correlation of Farabee and Casarella [9]. The data plotted in their Fig. 2 is replotted here as Fig. 4. The rms values from the current LES calculations are included and are consistent with the experimental data.

In a boundary layer with $Re_{\delta^*} = 1950$, Schewe [7] found that the skewness attained a value of approximately -0.2 with his smallest pressure transducer. When the diameter of the transducer was as large as 75 wall units, the skewness was essentially 0 and remained 0 when measured with larger transducers. Because the minimum resolved structure in the low-resolution LES has a streamwise extent of approximately 100 wall units and a spanwise extent of approximately 32 wall units, the expected value of the skewness should be 0. Although the slightly positive value of the skewness from the low-resolution calculation was unexpected, its near-zero value could easily be a consequence of the limited time series, especially in view of the relatively large value of the standard deviation of the skewness. The slightly negative value obtained with the high-resolution LES is closer to 0 than would be expected from Schewe's data [7]; however, the standard deviation is again large. In the turbulent channel-flow calculations of Chang, Abraham, and Piomelli [10], the variation in the skewness exceeded 0.2, and one well-resolved DNS computation had a positive skewness as large as 0.119; hence, the currently obtained values are well within the skewness variation of the prior work.

The flatness values obtained from the calculations are somewhat less than those obtained in the calculations of Ref. [10] and greater than what would be expected from Fig. 5 of Schewe [7], based on the minimum resolved scales of the LES. The close agreement between the values of the flatness for the two different resolutions used here and the similarly close agreement of the flatness for all five calculations reported by Chang, Abraham, and Piomelli [10], point to a possible Reynolds-number dependence of the flatness, with an approach to the Gaussian limit as the Reynolds number increases. In any case, the values computed indicate that high-amplitude infrequent events occur more often than what would be expected if the wall-pressure distribution were entirely Gaussian.

The coherence functions of the two-point spatial correlations are plotted in Figs. 5 and 6 for streamwise and spanwise separations, respectively. Although the general features of the coherence are reproduced with both high- and low-resolution calculations, the details are dependent on the resolution. Both calculations show that the streamwise correlation becomes and remains slightly negative with separation distances greater than approximately $3.5\delta^*$ (i.e., about 500 wall units). This behavior is consistent with most of the low-speed data that was reviewed and plotted by Bies [27]. However, with $\xi^+ < 150$, a much smoother curve is obtained with the high-resolution calculation. The low-resolution data appear to oscillate with a period of three points. The reason for this oscillation is not yet known. The spanwise correlation distance is much greater than the streamwise correlation distance. After a rapid decrease in the first few displacement thicknesses, the coherence function becomes nearly flat, with a value of approximately 0.05. As with the streamwise coherence function, the initial decay of the coherence of the high-resolution data is more severe than that of the low-resolution data. Although the same general trend of the spanwise coherence function is indicated by Corcos [3, 4] and Bies [27], the coherences of the data they plotted are generally slightly greater than either of the coherences presented here. Because the data from the high-resolution simulation decay more rapidly than the data from the low-resolution simulation, the slightly greater coherence from the experiments plotted by Corcos [3, 4] and Bies [27] may be a consequence of inadequate spatial resolution in the experiments.

3.2 Spectra

3.2.1 1-D power spectral density

The 1-D power spectral densities as functions of frequency for both high- and low-resolution calculations are plotted in Figs. 7(a) and (b). Figure 7(a) shows the spectral density normalized with outer-flow variables; Figure 7(b) shows the same data normalized with inner flow variables. The inner flow variables emphasize the high-frequency regime. Numerical roundoff error terminates the decay of the spectra at similar levels for both grid resolutions. The data are consistent with the findings of Schewe (see Fig. 10 in Ref. [7]); that is, the decay of the power spectral density of larger pressure transducers (which correspond here to the low-resolution calculation) occurs at a lower frequency and is steeper than the decay observed with smaller pressure transducers (which correspond here to the high-resolution calculation). The exponential decay that was observed by Schewe [7] of the spectra at high frequencies is clearly observed here in Fig. 7(b).

In Fig. 7(a), the high-resolution calculation maintains significant levels of the spectral density to a higher frequency than the low-resolution calculation. The higher mean-square pressure in Table 1 for the high-resolution calculation is at least partly a consequence of the extra high-frequency power that is resolved with the finer grid.

Farabee and Casarella [9] distinguish three regimes in the pressure spectral density. Their low-frequency regime where the spectrum scales with ω^2 , occurs with $\omega\delta^*/U_0 < 0.03$. For the computed flow, this corresponds to $\omega\delta^*/U_\tau < 0.75$. Such a small frequency is below the frequency resolution in the calculation, so the lack of an ω^2 regime is not surprising. The high-frequency regime observed by Farabee and Casarella [9] decays rapidly with frequency. This regime also exists in the current calculations and is clearly seen in Figs. 7(a) and 7(b). The maximum in the spectra occurs in the mid-frequency regime. The data of Farabee and Casarella [9] show that the maximum occurs at $\omega\delta/u_\tau = 50$, which corresponds to $\omega\delta^*/u_\tau \approx 6.5$ in the computed flow. Figure 7(a) and the supporting LES data suggest that, for both resolutions, the global maximum is $\omega\delta^*/u_\tau \approx 2.2$ and a secondary maximum exists in the vicinity of $\omega\delta^*/u_\tau \approx 5.6$. The discrepancy between the LES and the experiments as to the frequency of the maximum might be attributable to the streamwise-domain size of the calculation. If a disturbance with the frequency $\omega\delta^*/u_\tau = 2.2$ travels with a convection velocity of $U_c/u_\tau = 16.5$ (a reasonable value), then the wavelength of the disturbance would closely approximate the length of the computational domain. Because the computational domain is periodic, disturbances that have the appropriate combination of frequency and convection velocity (such that the wavelength equals the length of the streamwise domain), will be perfectly correlated. Chang, Abraham, and Piomelli [10] note that a similar anomalous peak in the spectrum appears in their simulation that has the shortest streamwise domain. A careful study of their data also reveals the presence of spectral peaks at frequencies associated with the domain size for most of their other simulations. Only their calculation with the longest streamwise domain does not show a local peak at the relevant frequency. In this case however, the spectrum does not exhibit the anticipated decrease in amplitude at the relevant frequency; hence, even in this calculation, the amplitude of the spectrum at a particular frequency appears to be contaminated by a numerical artifact. A future computation will be performed to further clarify this issue. However, in all cases, the numerically introduced error appears to be narrowly confined in frequency space and the bulk of the results are reliable.

3.2.2 2-D frequency–streamwise-wavenumber spectral density

Contours of the spectral density as functions of the frequency and streamwise wavenumber are plotted for the low-resolution simulation in Fig. 8 and for the high-resolution calculation in Figs. 9(a) and 9(b). All resolved wavenumbers are included in Figs. 8 and 9(a). In Fig. 9(b), the data from the high-resolution calculation are plotted for the same range of wavenumbers and frequencies that was used for the plot of the low-resolution data in Fig. 8. The convective ridge can easily be identified in all plots as the elongated crest of maximum spectral density in frequency–streamwise-wavenumber space. The slope of this crest is often used as a measure of the convection velocity U_c . The considerably smoother contours in Fig. 8 relative to those in Figs. 9(a) and 9(b) are a consequence of the more extensive time sample that was available for the low-resolution calculation. The small power buildups around the zero wavenumber that are observed at high frequencies were also observed in the calculations of Choi and Moin [6] and Chang, Abraham, and Piomelli [10]. The meaning of the power buildups is not clear, but the very small amplitude and the high frequency at which they first become noticeable suggests that they have minimal impact on the quantities of concern here.

The connection between the spatial and temporal resolutions can be investigated through a comparison of Figs. 8 and 9(a). Because power is concentrated in the convective ridge, estimation of the temporal spectral density is only accurate up to those frequencies for which the convective ridge is spatially resolved. At higher frequencies, the convective ridge will be incomplete or will be missing entirely. Hence, the temporal spectral densities at these higher frequencies will lack a significant component of power that should be included. Figure 8 shows that resolution of the convective ridge to the -30 -dB contour occurs up to a frequency of $\omega\delta^*/u_\tau \approx 27$. In the high-resolution calculation, Fig. 9(a) shows that the resolution of the -30 -dB contour extends up to $\omega\delta^*/u_\tau \approx 75$. At higher frequencies, a significant portion of the power in the convective ridge will not be included in the estimate of temporal power spectral density.

Careful comparison of Figs. 8 and 9(b) indicates that the crest of the convective ridge is accurately computed in the low-resolution simulation up to the limit of the maximum streamwise wavenumber. However, away from the crest, the low-resolution calculation experiences a more rapid decrease in power than the high-resolution calculation. The cause of this phenomenon is not clear.

3.2.3 Streamwise cross-spectral density

The streamwise coherence of the cross-spectral density function can be studied as a function of the phase $\alpha = \omega\xi/U_c$. The phase can be altered by varying either the frequency or the separation distance. In Figs. 10(a) and 10(b), each line represents the coherence of the cross-spectral density for a fixed separation distance ξ/δ^* . In the low-resolution case, the smallest separation distances show steep increases in the coherence for their highest frequencies. These steep increases are artifacts of the limited spatial resolution. Although some scatter exists, except for the smallest separation distances the high-frequency data form a curve that is independent of separation distance. The thick solid line in the figures is the function $\exp(-c_1|\omega\xi/U_c|)$, where the value of c_1 is chosen to be 0.145, which is the same value used by Farabee and Casarella [9] at a slightly greater Reynolds number. Note that in Figs. 10(a) and 10(b), as $\omega\xi/U_c \rightarrow 0$, the coherence does not uniformly tend to unity. Instead, the coherence is rapidly reduced with a different zero-frequency level attained by each separation distance. Farabee and Casarella [9] also observed

this behavior for data at low frequencies. For coherence to be maintained at the low frequencies, the low-frequency pressure field would need to remain correlated over enormous streamwise distances. As Farabee and Casarella [9] state, “This would require that the turbulence activities producing the wall pressure fluctuations convect over equally long distances without becoming distorted by the mean velocity gradient or turbulence mixing in the flow.”

The coherence versus phase relationship can also be studied by plotting lines of constant frequency while the separation distance varies. In this representation, as $\xi \rightarrow 0$ the coherence must tend toward unity. Figures 11(a) and 11(b) show the coherence of lines of constant frequency for the high- and low-resolution data. The thick solid line is again the function $\exp(-c_1|\omega\xi/U_c|)$ with the value of c_1 chosen to be 0.145. The high-frequency curves of the low-resolution data show significant departures from the rest of the data. However, the five highest frequencies are all above the intercept of the -30 -dB contour with the maximum resolved streamwise wavenumber, as can be seen in Fig. 8; hence, at best the five highest frequencies are marginally resolved. In the high-resolution data, all frequencies shown are adequately resolved. Farabee and Casarella [9] observed a slight increase in the decay rate with an increase in frequency; Figure 11(a) provides some support for this conclusion. In addition, they observed a low-frequency cutoff of $\omega\delta/u_\tau = 50$, below which the coherence curves were no longer similar. Because $\delta \approx 8\delta^*$, the curves that represent the lowest frequency (circles) in Figs. 11(a) and (b) are well below the cutoff. The behavior of the low-frequency curves with respect to the “universal” curve is consistent with the observations of Farabee and Casarella [9].

3.2.4 Convection velocity

The convection velocity can be determined from the phase of the streamwise cross-spectral density as $U_c = \omega\xi/\alpha$. For the two resolutions used, Figs. 12(a) and 12(b) illustrate the dependence of the convection velocity on separation distance for a variety of different frequencies that are at least marginally resolved. The lowest sampled frequency, $\omega\delta^*/u_\tau \approx 1.12$, has an unusually low convection velocity. However, this frequency is below the cutoff frequency for similarity; hence, the anomalous behavior is not unexpected. In the limit of zero separation distance, the convection velocity for most of the frequencies tends toward a value between $0.55U_0$ (approximately $13.3u_\tau$) and $0.60U_0$ (approximately $14.5u_\tau$). These values are approximately 10 percent less than the values obtained by Farabee and Casarella [9] at a Reynolds number that is approximately 10 percent greater than the Reynolds number of the computation. Their convection velocities for zero separation at another, greater Reynolds number are even higher, although not by the same proportion. Because the convection velocity is limited by the free-stream speed, any monotonic Reynolds-number dependence must eventually asymptote to some value, although what that value should be is not clear from the data.

The convection velocity generally increases slowly with increasing separation distance. This trend is clearly seen in Figs. 13(a) and 13(b), which show the convection velocities as functions of frequency for different separation distances. The thick solid line is an estimate of the $\xi = 0$ curve. This curve was obtained through the use of L’Hospital’s rule; that is,

$$U_c(\omega)_{\xi=0} = \lim_{\xi \rightarrow 0} \frac{\omega\xi}{\alpha} = \omega / \left(\frac{\partial\alpha}{\partial\xi} \right)_{\xi=0} \quad (24)$$

where $\partial\alpha/\partial\xi$ was computed with second-order forward differences. The curves with $\xi/\delta^* = 0.467$ are almost identical to the extrapolated $\xi = 0$ curves. The trend of increasing convection velocity

with separation distance is also observed by Farabee and Casarella [9]. The higher frequency data are poorly resolved in the low-resolution calculation. For small separation distances, the almost linear growth of the convection velocity with frequency is a direct consequence of the spatial resolution limitations in the streamwise direction.

3.2.5 Spanwise cross-spectral density

The spanwise cross-spectral density is essentially a real-valued function; hence, a plot of coherence versus the phase would not be useful. Corcos [3, 4] suggested that a similarity variable $\omega\eta/U_c$ would collapse the coherence data. Although U_c (as derived from the phase of the streamwise cross-spectral density) depends weakly on both the streamwise separation distance and the frequency (for use in forming the spanwise similarity variable), U_c can be approximated by its dependence on the frequency with zero streamwise separation.

As with the streamwise cross-spectral density, the similarity variable $\omega\eta/U_c$ can be varied by changing either the frequency or the separation distance and holding the other fixed. Figures 14(a) and 14(b) show curves of spanwise coherence for various spanwise separations as functions of the frequency. The coherence as $\omega \rightarrow 0$ clearly show a strong decrease for the low-resolution calculation; for the high-resolution calculation, the data shows a great deal of jitter in this region. The thick solid line represents a curve $\exp(-0.8 \omega\eta/U_c)$. This curve seems to overestimate the coherence for low values of $\omega\eta/U_c$ and underestimate the coherence for high values of $\omega\eta/U_c$; hence, a simple exponential does not fit these data well. Figures 15(a) and 15(b) show curves of spanwise coherence for various frequencies as functions of the spanwise separation. The lowest frequency curves show significant departures from the remaining curves. Similar behavior of the low-frequency data was observed for the streamwise cross-spectral density in Figs. 11(a) and 11(b). The same exponential curve fit that was used in Figs. 14(a) and 14(b) is inadequate here also.

In Figs. 16(a), 16(b), and 17(a), and 17(b) a new single parameter curve is introduced that provides a better fit to the data. Rather than an exponential function, the modified inverse square function $C_s^2/[C_s^2 + (\omega\eta/U_c)^2]$ is used. A value $C_s = 0.9$ produces the thick solid curve in the figures. For low values of the similarity parameter, the function was chosen to better fit the cases in which $\eta \rightarrow 0$ (for which the correct asymptotic behavior is known) rather than $\omega \rightarrow 0$. Because the function involves just one parameter, the allowance of the parameter C_s to be a function of the flow conditions might lead to straightforward curve fitting of similar data are collected under different conditions (e.g., different Reynolds numbers or pressure gradients).

4 Conclusions

Statistical properties of the wall-pressure fluctuations were investigated for a turbulent boundary layer with $Re_{\delta^*} = 3500$. The data were produced by large-eddy simulation with two different grid resolutions. Although the global flow properties were quite similar, the high-resolution calculation more accurately captured higher temporal frequencies of the wall-pressure fluctuations. However, the increased time series available with the low-resolution calculation considerably decreased the jitter in a number of plots in comparison with the high-resolution computation.

The globally averaged quantities of mean-square wall pressure, skewness, and flatness for the two resolutions have values that are approximately within a single standard deviation of

each other. The actual values reveal that the distribution of wall-pressure is not Gaussian; the occurrence of large-amplitude wall-pressure events is more likely than would be expected for a Gaussian distribution. This conclusion is in accordance with those of previous experiments and calculations.

The coherence of the time-averaged two-point correlations behaves similarly for both resolutions although the streamwise correlation computed with low resolution has a small-amplitude three-point oscillation while the correlation computed with high resolution is smooth. The coherence functions from both resolutions become and remain slightly negative for distances greater than about $3.5\delta^*$. The spanwise two-point correlations are considerably broader with no apparent oscillations with either the low- or high-resolution calculations.

The one-dimensional frequency spectra are generally consistent with previous experimental and computational studies. An artificial peak in the spectrum at $\omega\delta^*/u_\tau \approx 2.2$ is probably an artifact of the length of the computational domain. Discrepancies associated with this computational issue appear to be narrowly confined in frequency space. The results with the coarser grid resolution are similar to results that are obtained with larger sized transducers in physical experiments. Spectra plotted as functions of frequency and streamwise wavenumber show that the crest of the convective ridge is resolved to the highest streamwise wavenumber available in both calculations. The decay of the spectra away from the ridge is more rapid in the low-resolution calculation than in the high-resolution calculation.

The coherences of the cross-spectral density functions have similar forms in both calculations. The streamwise and spanwise coherence functions are smoother when lines of constant frequency are considered, and the independent variable varies due to changes in the separation distances. Farabee and Casarella [9] suggest that a low-frequency cutoff of $\omega\delta^*/u_\tau \approx 6.5$ determines the lower limit for the similarity behavior of the cross-spectral density. This value of the cutoff is consistent with the data presented here. The similarity curve for the streamwise coherence is fit quite well by an exponential with the same decay rate used by Farabee and Casarella [9] in their experimental studies (with a slightly greater Reynolds number). The spanwise coherence could not be fit with a simple exponential function. Instead, a single-parameter modification to an inverse-square function was developed to fit the data. The parameter can be made a function of the flow conditions. Future work will help determine its value for other flow conditions.

The calculations reveal that the general results from the low-resolution calculations are consistent with those of the higher resolution calculation, especially when attention is confined to the frequency range that is most important for structural vibrations of an aircraft fuselage.

5 Acknowledgments

The author thanks Mr. Peter Chang for much useful information, Prof. Ugo Piomelli for guidance on the implementation of the subgrid-scale model, Dr. Philippe Spalart for advice with regard to the multiple-scales approach, Dr. Thomas Zang for providing an initial turbulent flow field, and Drs. Jay Robinson and Craig Streett for many additional useful suggestions. The author also thanks Dr. Thomas Farabee for providing tabulated experimental data. This work was performed in the Fluid Mechanics and Acoustics Division of NASA Langley Research Center under contract NAS1-20059.

References

- [1] Blake, W., *Mechanics of Flow-Induced Sound and Vibration, Vol. II*, Academic Press, 644 (1986).
- [2] Wilby, J. F. and Gloyna, F. L., "Vibration measurements of an airplane fuselage structure: 1. Turbulent boundary layer excitation," *J. Sound and Vibration* **25**, 443 (1972).
- [3] Corcos, G. M., "Resolution of pressure in turbulence," *The J. of the Acoustical Soc. of America* **35**, 192 (1963).
- [4] Corcos, G. M., "The structure of the turbulent pressure field in boundary-layer flows," *J. Fluid Mech.* **18**, 353 (1963).
- [5] Kim, J., "On the structure of pressure fluctuations in simulated turbulent channel flow," *J. Fluid Mech.* **205**, 421 (1989).
- [6] Choi, H. and Moin, P., "On the space-time characteristics of wall-pressure fluctuations," *Phys. Fluids A* **2**, 1450 (1990).
- [7] Schewe, G., "On the structure and resolution of wall-pressure fluctuations associated with turbulent boundary-layer flow," *J. Fluid. Mech.* **134**, 311 (1983).
- [8] Efimtsov, B. M., "Characteristics of the field of turbulent wall pressure fluctuations at large Reynolds numbers," *Sov. Phys. Acoust.* **28**, 289 (1982).
- [9] Farabee, T. M. and Casarella, M. J., "Spectral features of wall pressure fluctuations beneath turbulent boundary layers," *Phys. Fluids A* **3**, 2410 (1991).
- [10] Chang, P. A., Abraham, B. M., and Piomelli, U., "Wavenumber-frequency characteristics of wall pressure fluctuations computed using turbulence simulations," Presented at *Symposium on Active/Passive Control of Flow-Induced Vibration and Noise: 1994 International Mechanical Engineering Congress and Exposition* (1994).
- [11] Lilly, D. K., "A proposed modification of the Germano subgrid-scale closure method," *Phys. Fluids A* **4**, 633 (1992).
- [12] Germano, M., Piomelli, U., Moin, P., and Cabot, W. H., "A dynamic subgrid-scale eddy viscosity model," *Phys. Fluids A* **3**, 1760 (1991).
- [13] Zang, T. A. and Hussaini, M. Y., "On spectral multigrid methods for the time-dependent Navier-Stokes equations," *Appl. Math. Comp.* **19**, 359, (1986).
- [14] Spalart, P. R. and Leonard, A., "Direct numerical simulation of equilibrium turbulent boundary layers," *Turbulent Shear Flows 5*, Springer-Verlag (1987).
- [15] Spalart, P. R., "Direct simulation of a turbulent boundary layer up to $R_\theta = 1410$," *J. Fluid Mech.* **187**, 61 (1988).
- [16] Schlichting, H., *Boundary Layer Theory*, 7th edition, McGraw-Hill Book Company, New York (1979).

- [17] Press, W. H., Teukolsky, S. A., Vetterling, W. T., and Flannery, B. P., *Numerical Recipes in C*, 2nd ed., Cambridge University Press, New York (1992).
- [18] Hardin, J., "Introduction to time series analysis," NASA Ref. Pub. 1145 (1990).
- [19] Zang, T. A. and Hussaini, M. Y., "Multiple paths to subharmonic laminar breakdown in a boundary layer," *Physical Review Letters* **64**, 641 (1990).
- [20] Piomelli, U., "High Reynolds number calculations using the dynamic subgrid-scale stress model," *Phys. Fluids A* **5**, 1484 (1993).
- [21] Blake, W. J., "Turbulent boundary layer wall pressure fluctuations on smooth and rough walls," *J. Fluid Mech.* **44**, 637 (1970).
- [22] McGrath, B. E. and Simpson, R. L., "Some features of surface pressure fluctuations in turbulent boundary layers with zero and favorable pressure gradients," NASA CR 4051 (1987).
- [23] Bull, M. K. and Thomas, A. S. W., "High frequency wall-pressure fluctuations in turbulent boundary layers," *Phys. Fluids* **19**, 597 (1976).
- [24] Emmerling, R., Meier, G., and Dinkelacker, A., AGARD Conf. Proc. No. 131, p. 24-1(1973).
- [25] Lauchle, G. C. and Daniels, M. A., "Wall-pressure fluctuations in turbulent pipe flow," *Phys. Fluids* **30** 3019 (1987).
- [26] Horne, M., "Physical and computational investigation of wall-pressure fluctuations in channel flow," NRL Report 6628, April (1990).
- [27] Bies, D. A., "A review of flight and wind tunnel measurements of boundary layer pressure fluctuations and induced structural response," NASA CR-626 (1966).

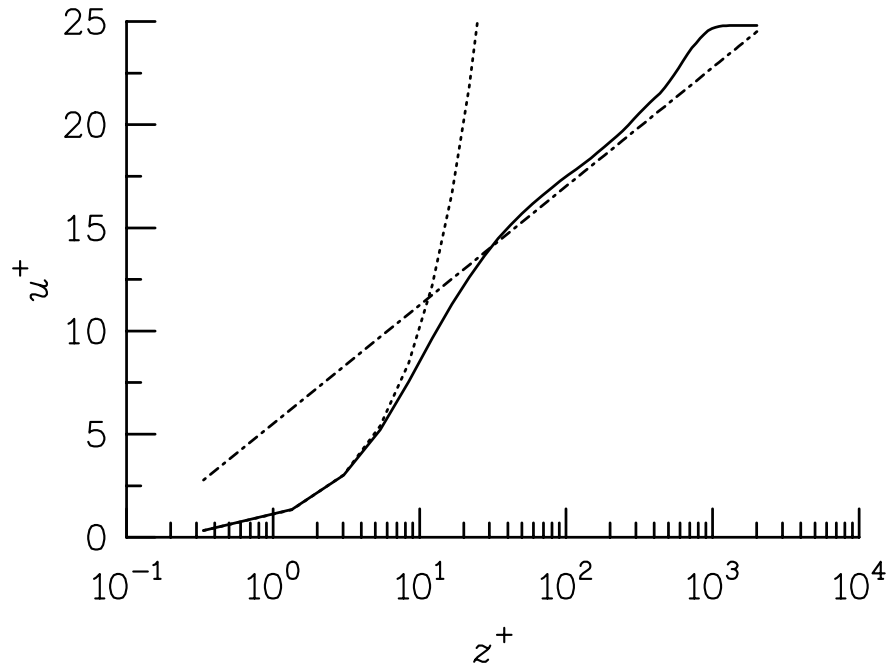


Figure 1. Mean-flow profile in wall coordinates at $t = 2460$. — LES; $u^+ = z^+$; -.-.-. $u^+ = 2.5 \log(z^+) + 5.5$

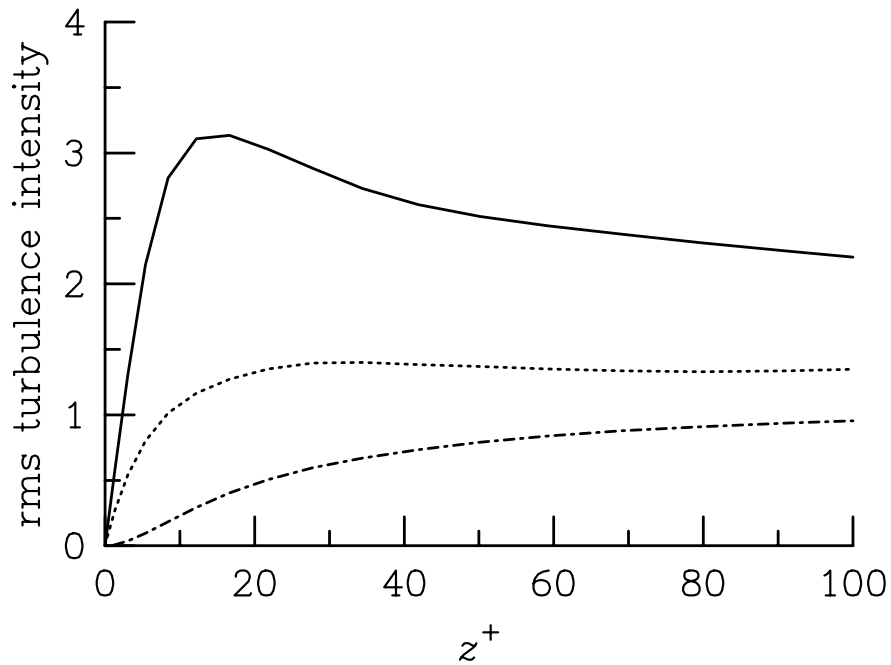
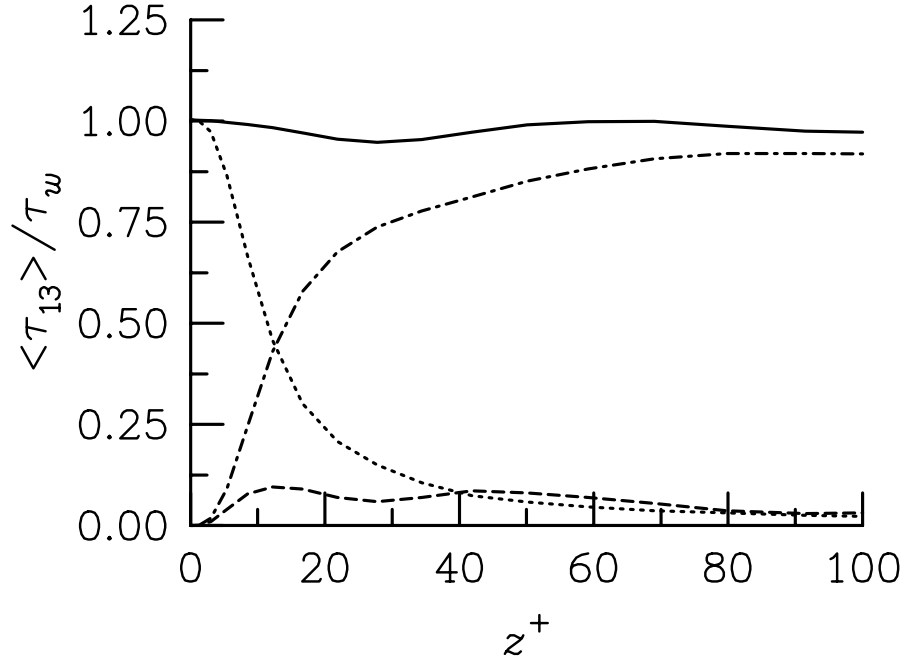
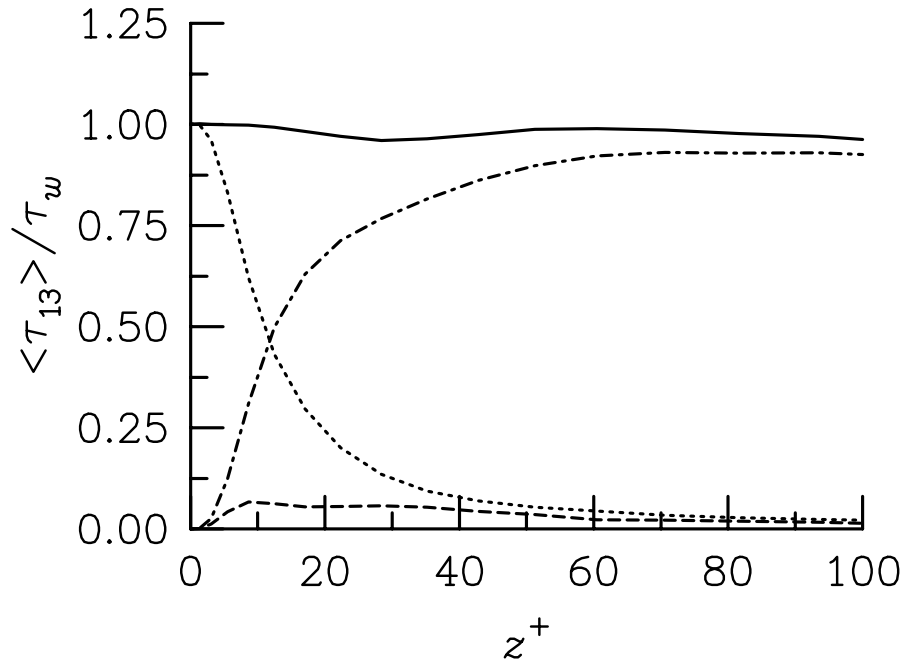


Figure 2. Turbulence intensity profiles at $t = 2460$. — u_{rms} v_{rms} -.-.-. w_{rms}



(a) Low resolution.



(b) High resolution.

Figure 3. Dominant turbulent shear stress profiles at $t = 2460$. — total; viscous; -.-.-.- turbulent resolved; --- turbulent SGS.

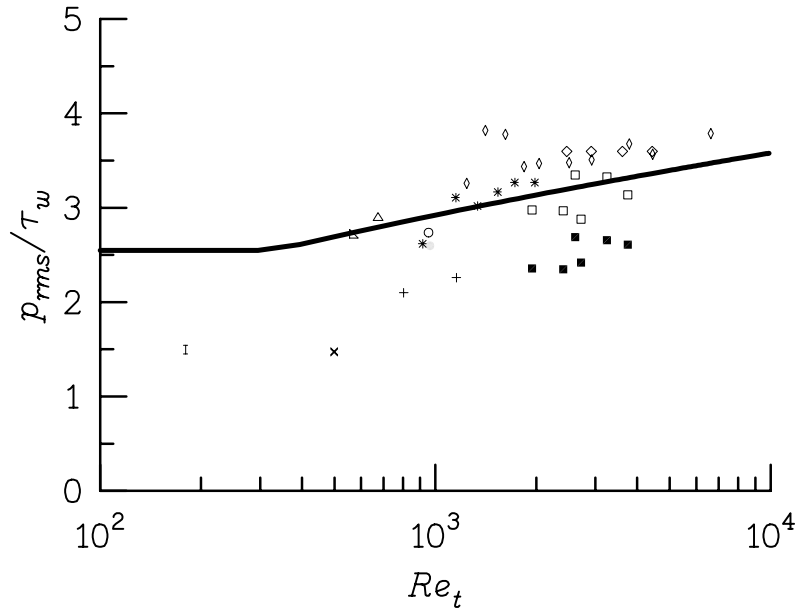
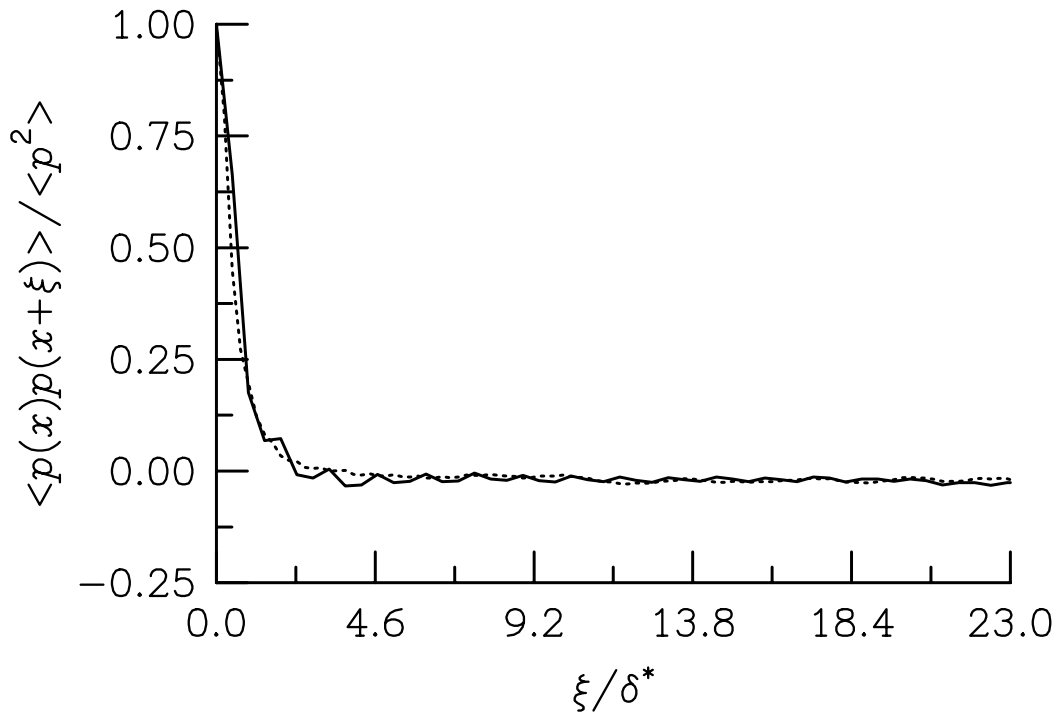
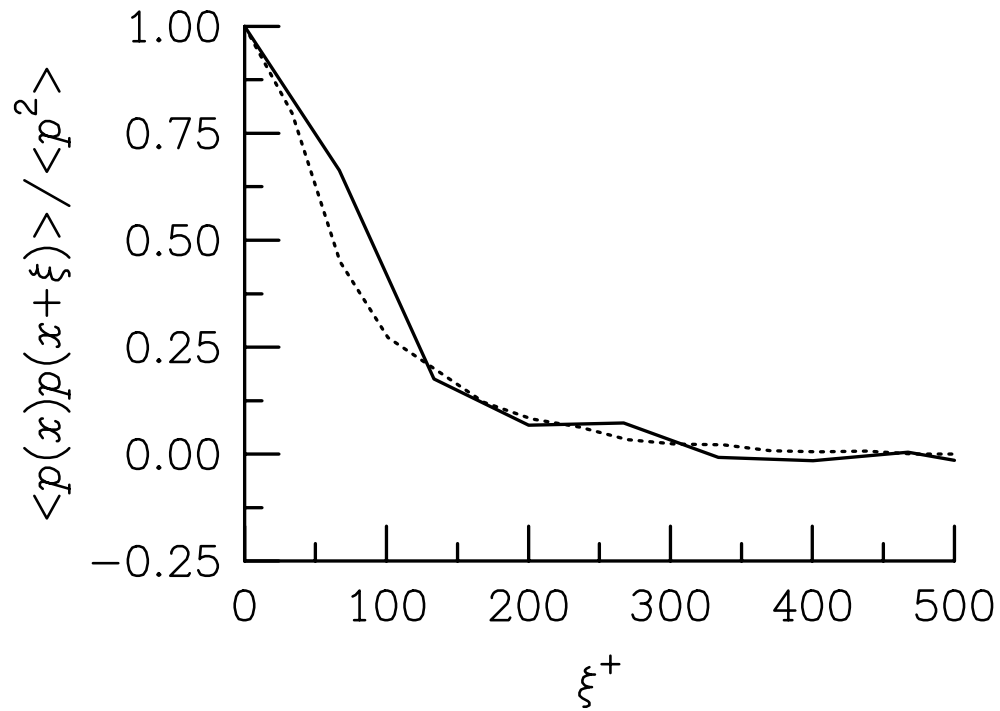


Figure 4. Variations in rms wall pressure as a function of Re_t . —Eq. (2) of Farabee and Casarella [9]; \circ current low-resolution LES; \bullet current high-resolution LES; $*$ Farabee and Casarella [9]; \diamond Blake [21]; \diamond McGrath and Simpson [22]; \square Bull and Thomas [23] open pinhole; \blacksquare Bull and Thomas [23] filled pinhole; \triangleright Schewe [7]; \triangleleft Emmerling, Meier, and Dinkelacker [24]; \times Lauchle and Daniels [25]; $+$ Horne [26]; $\bar{\mid}$ Choi and Moin [6].

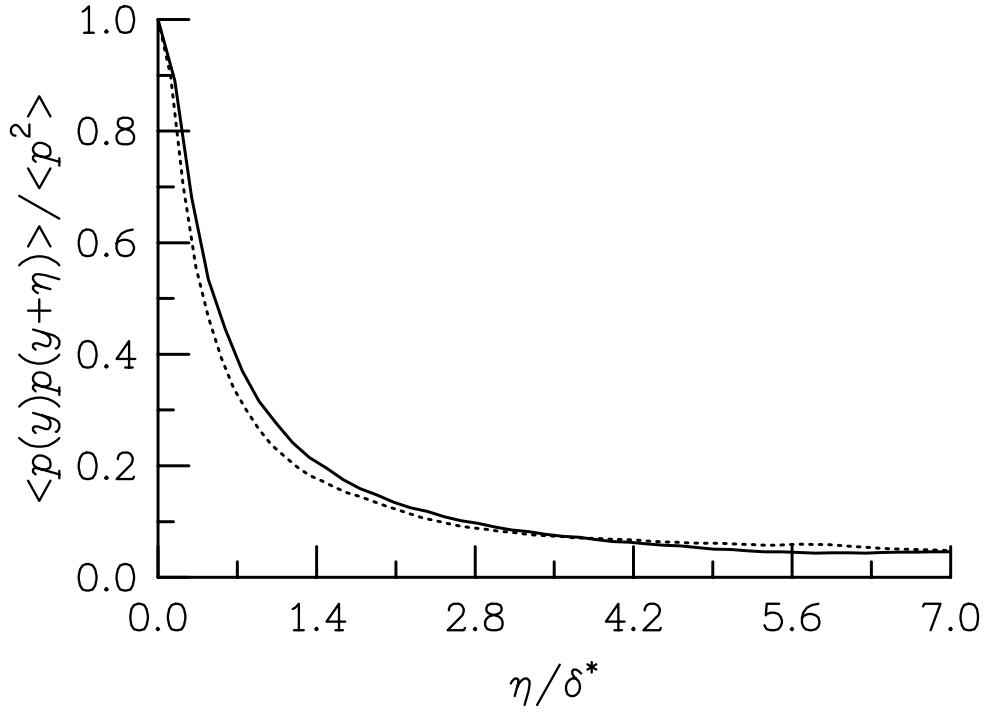


(a) Outer scales.

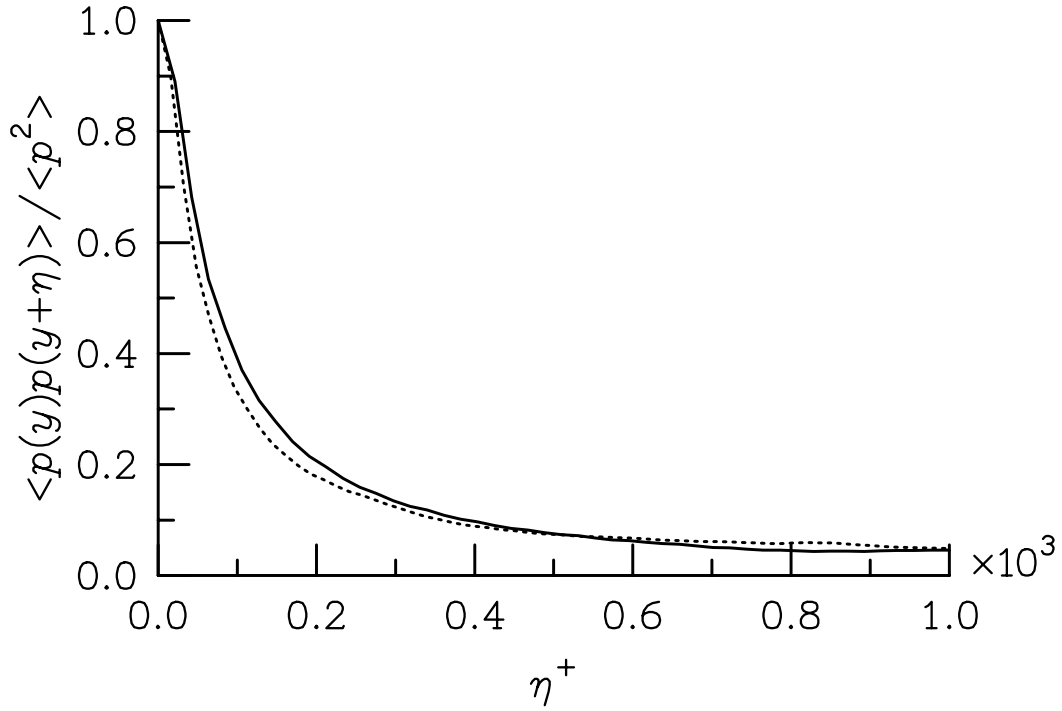


(b) Expanded view with inner scales.

Figure 5. Coherence of two-point streamwise correlation. — Low resolution; High resolution.

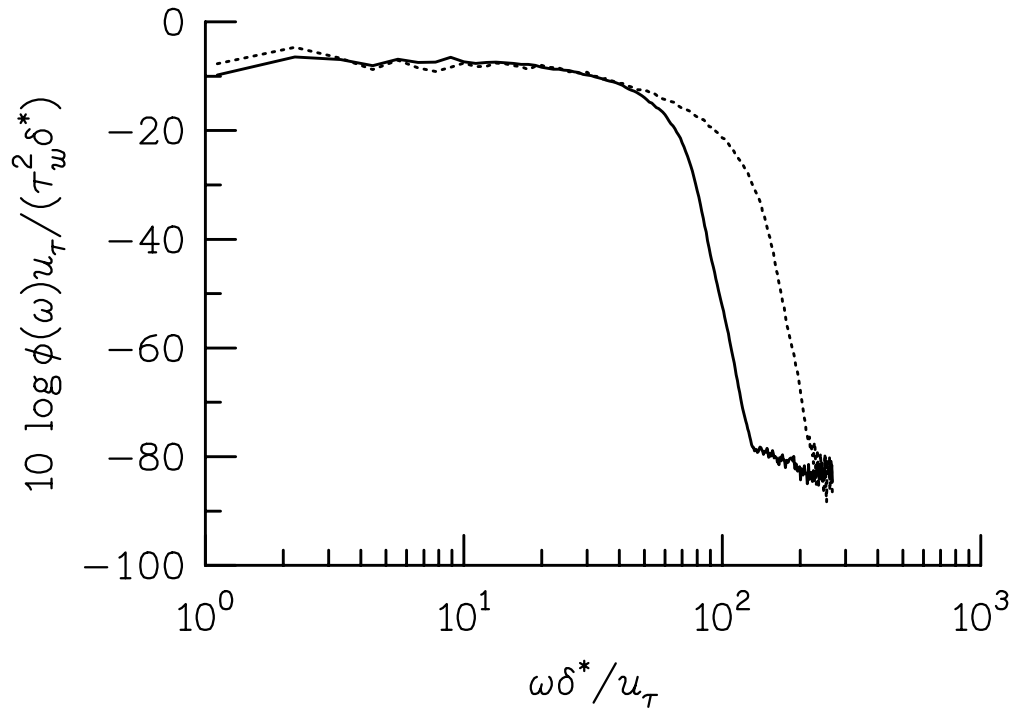


(a) Outer scales.

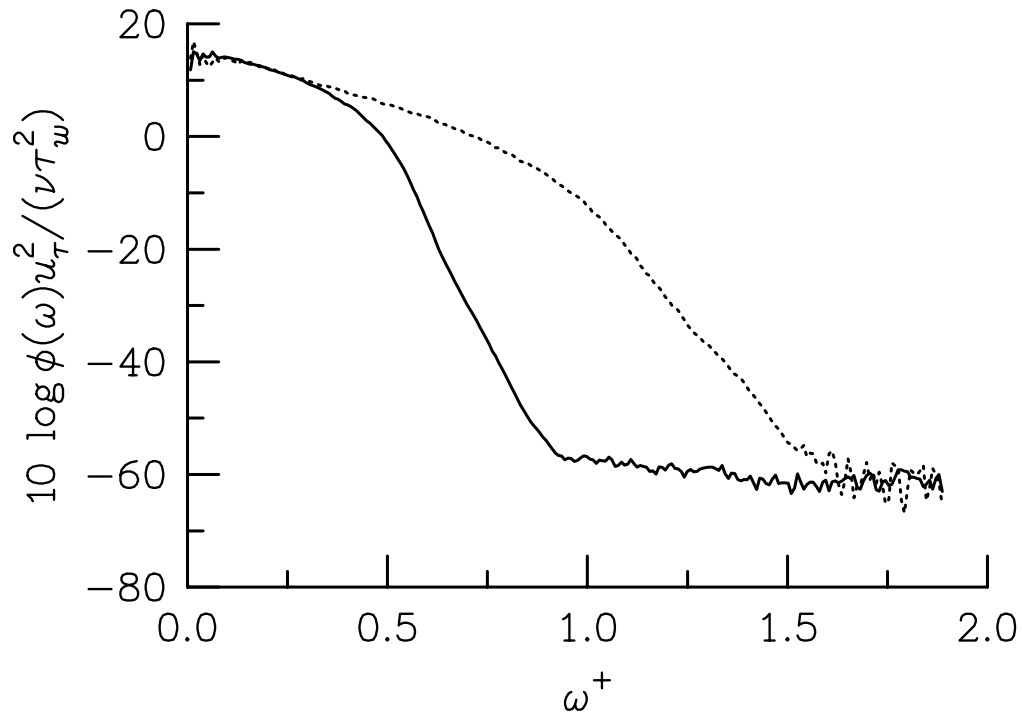


(b) Inner scales.

Figure 6. Coherence of two-point spanwise correlation. — Low resolution; High resolution.



(a) Outer scalings.



(b) Inner scalings.

Figure 7. Frequency spectrum. — Low resolution; High resolution.

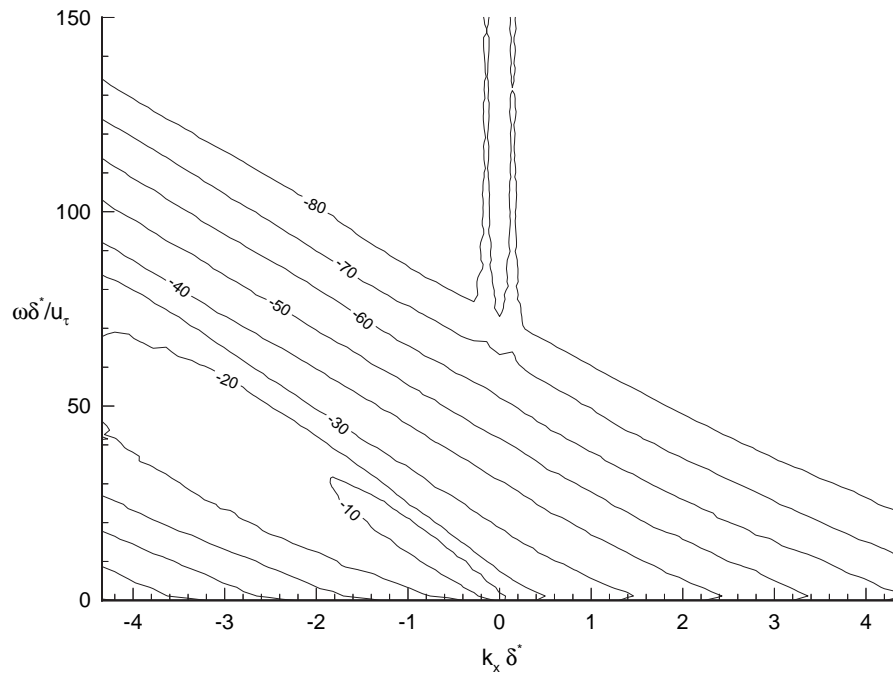
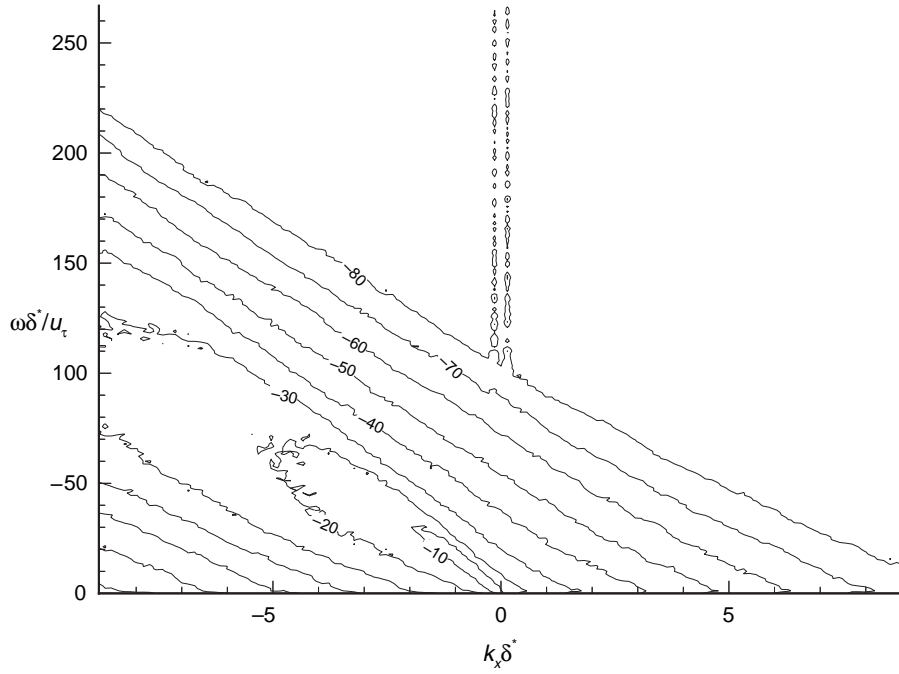
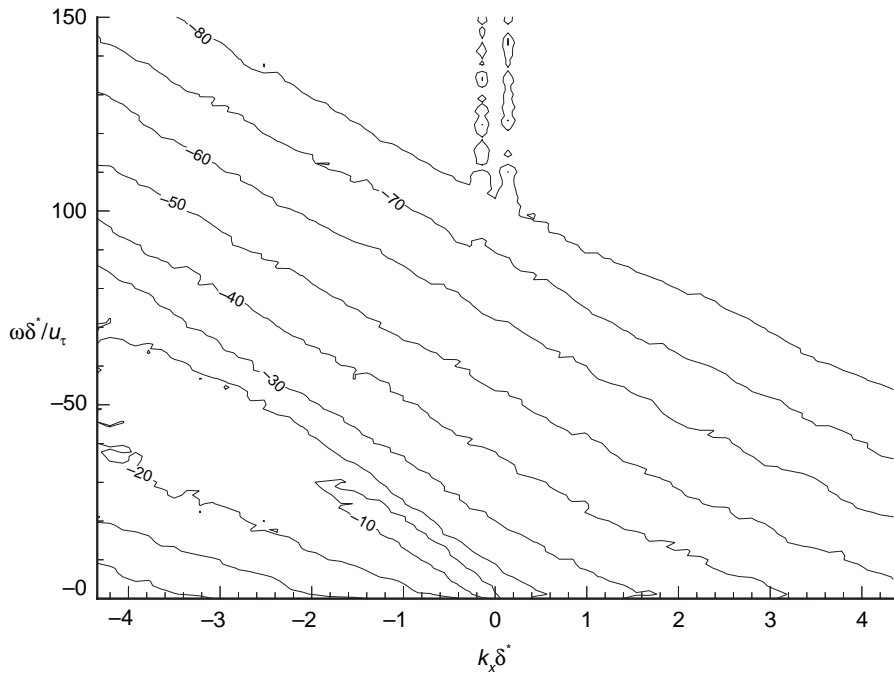


Figure 8. Contours of $10 \log[\phi(\omega, k_x) u_\tau / (\delta^* \tau_w)^2]$ as function of frequency and streamwise wavenumber (low resolution).

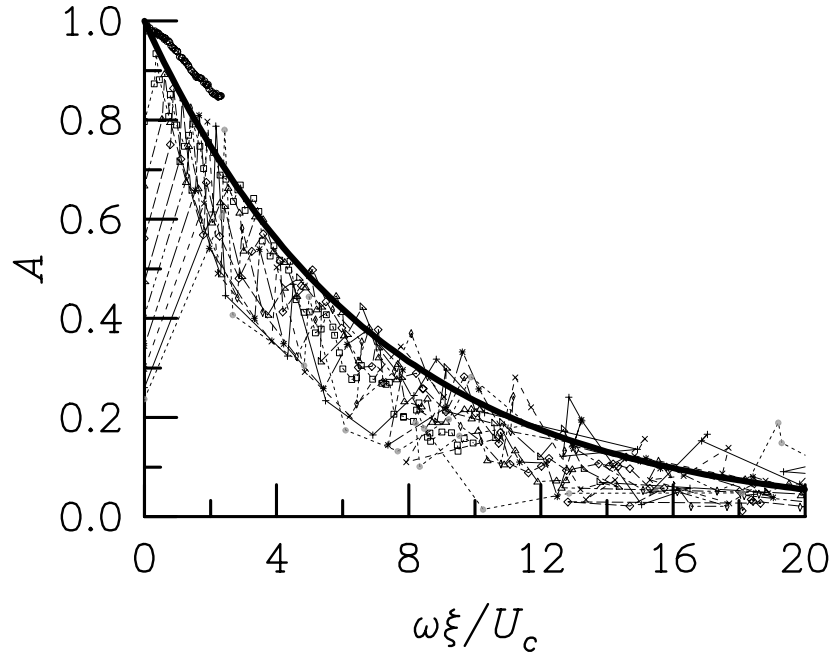


(a) All resolved wavenumbers plotted.

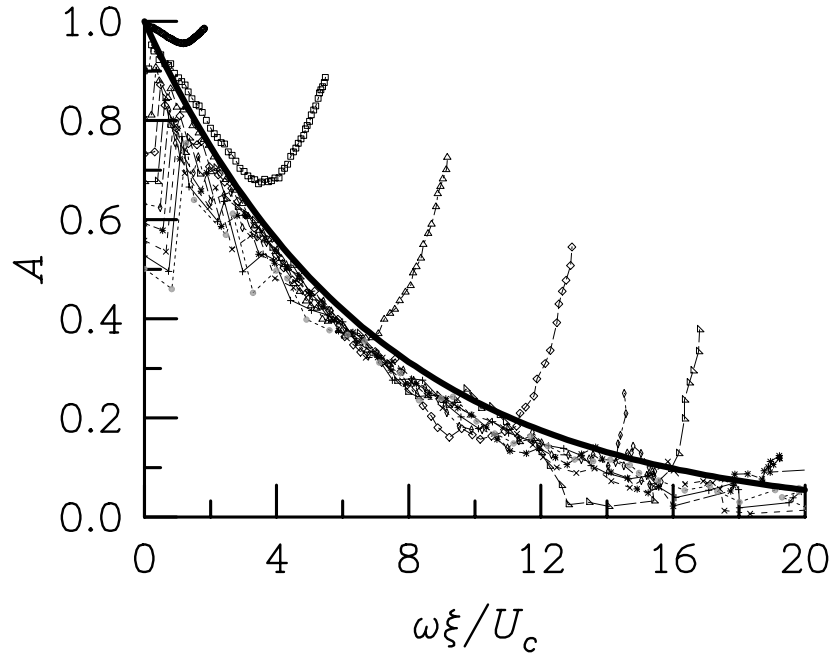


(b) Identical scale figure 7.

Figure 9. Contours of $10 \log[\phi(\omega, k_x)u_\tau / (\delta^* \tau_w)^2]$ as function of frequency and streamwise wavenumber. High resolution.

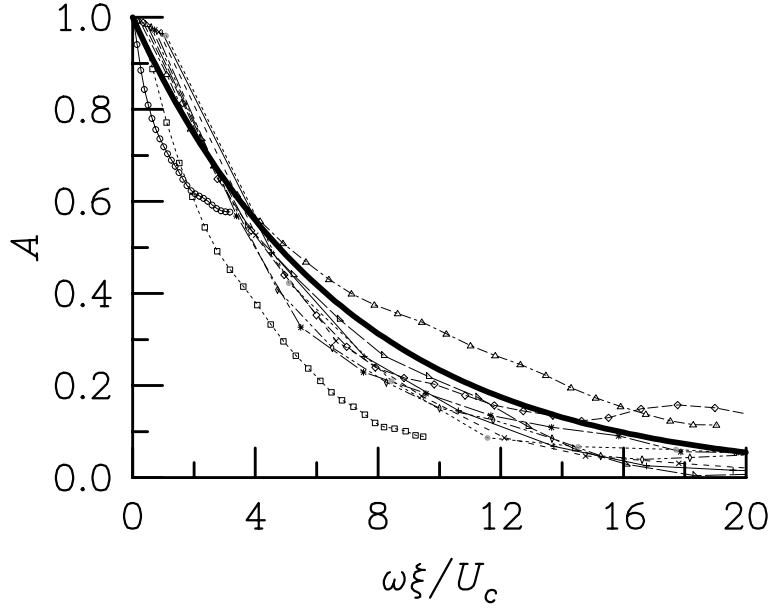


(a) High resolution.

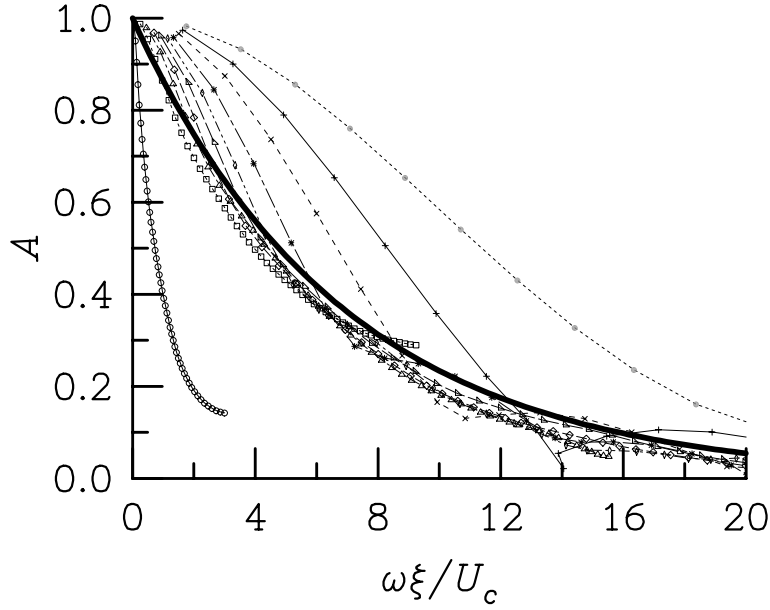


(b) Low resolution.

Figure 10. Streamwise coherence of cross-spectral density versus phase. Thick solid line is $\exp(-0.145|\omega\xi/U_c|)$. Symbols are curves for different separation distances. $\circ \xi/\delta^* = 0.47$; $\square \xi/\delta^* = 2.34$; $\triangle \xi/\delta^* = 4.21$; $\diamond \xi/\delta^* = 6.08$; $\triangleright \xi/\delta^* = 7.95$; $\diamond \xi/\delta^* = 9.82$; $* \xi/\delta^* = 11.69$; $\times \xi/\delta^* = 13.56$; $+ \xi/\delta^* = 15.43$; $\bullet \xi/\delta^* = 17.30$.

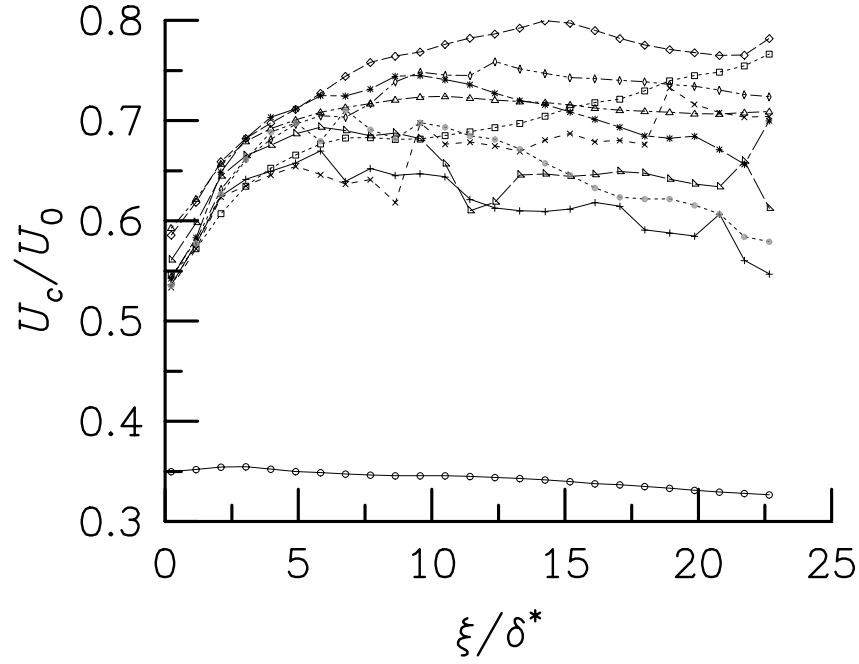


(a) High resolution. $\circ \omega\delta^*/u_\tau = 1.11$; $\square \omega\delta^*/u_\tau = 7.78$; $\triangle \omega\delta^*/u_\tau = 14.46$; $\diamond \omega\delta^*/u_\tau = 21.13$; $\triangleright \omega\delta^*/u_\tau = 27.80$; $\diamond \omega\delta^*/u_\tau = 34.47$; $* \omega\delta^*/u_\tau = 41.14$; $\times \omega\delta^*/u_\tau = 47.81$; $+ \omega\delta^*/u_\tau = 54.49$; $\bullet \omega\delta^*/u_\tau = 61.16$.

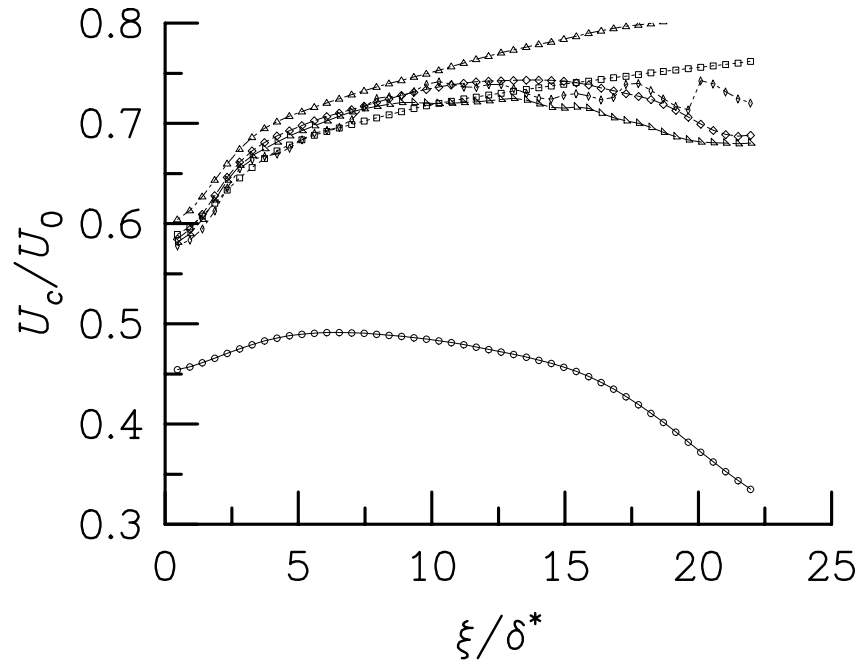


(b) Low resolution. $\circ \omega\delta^*/u_\tau = 1.12$; $\square \omega\delta^*/u_\tau = 7.86$; $\triangle \omega\delta^*/u_\tau = 14.59$; $\diamond \omega\delta^*/u_\tau = 21.33$; $\triangleright \omega\delta^*/u_\tau = 28.07$; $\diamond \omega\delta^*/u_\tau = 34.81$; $* \omega\delta^*/u_\tau = 41.55$; $\times \omega\delta^*/u_\tau = 48.29$; $+ \omega\delta^*/u_\tau = 55.02$; $\bullet \omega\delta^*/u_\tau = 61.76$.

Figure 11. Streamwise coherence of cross-spectral density versus phase. Thick solid line is $\exp(-0.145|\omega\xi/U_c|)$. Symbols are curves for different frequencies.

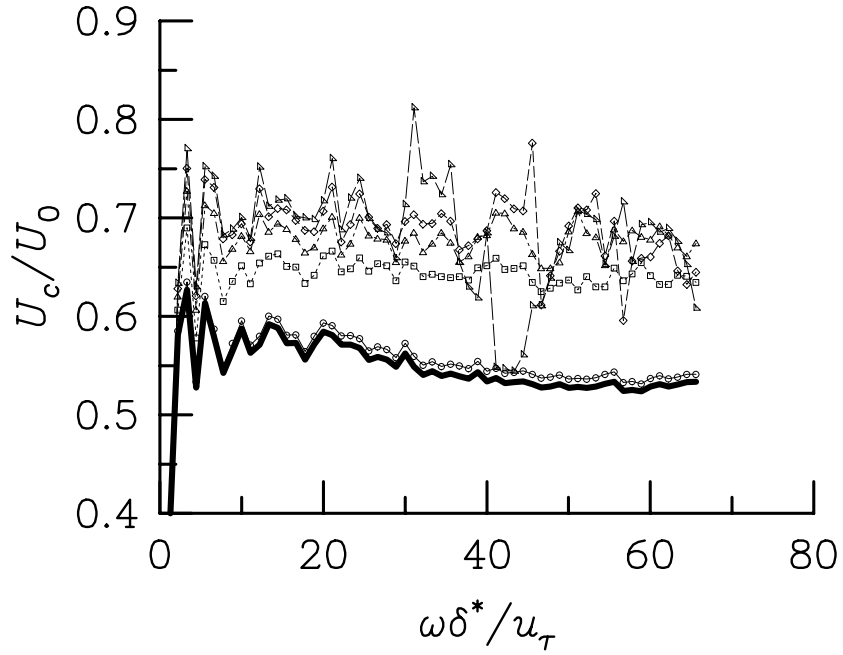


(a) High resolution. $\circ \omega\delta^*/u_\tau = 1.11$; $\square \omega\delta^*/u_\tau = 7.78$; $\triangle \omega\delta^*/u_\tau = 14.46$; $\diamond \omega\delta^*/u_\tau = 21.13$; $\triangleright \omega\delta^*/u_\tau = 27.80$; $\diamond \omega\delta^*/u_\tau = 34.47$; $*$ $\omega\delta^*/u_\tau = 41.14$; $\times \omega\delta^*/u_\tau = 47.81$; $+$ $\omega\delta^*/u_\tau = 54.49$; $\bullet \omega\delta^*/u_\tau = 61.16$.

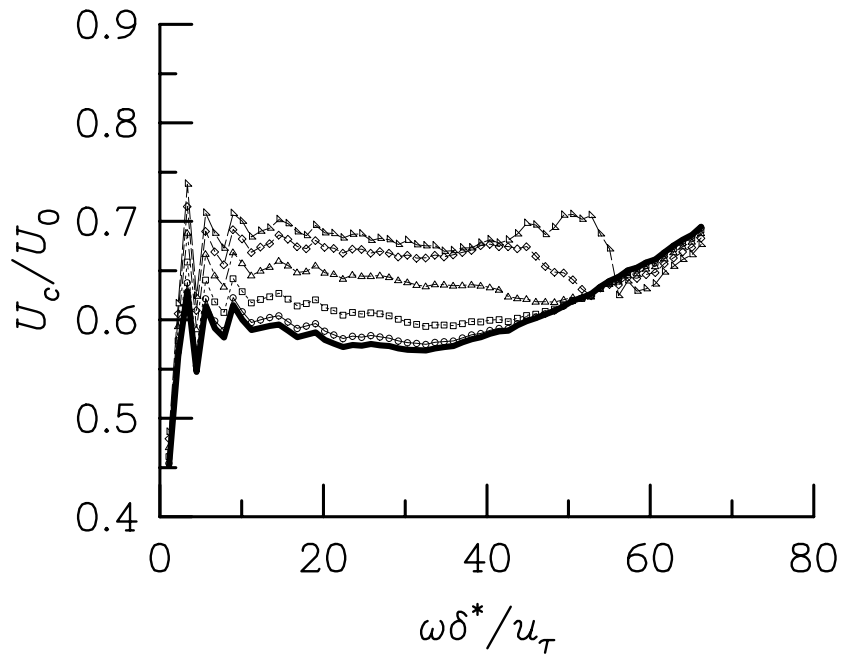


(b) Low resolution. $\circ \omega\delta^*/u_\tau = 1.12$; $\square \omega\delta^*/u_\tau = 7.86$; $\triangle \omega\delta^*/u_\tau = 14.59$; $\diamond \omega\delta^*/u_\tau = 21.33$; $\triangleright \omega\delta^*/u_\tau = 28.07$; $\diamond \omega\delta^*/u_\tau = 34.81$.

Figure 12. Convection velocity as function of separation for different frequencies.

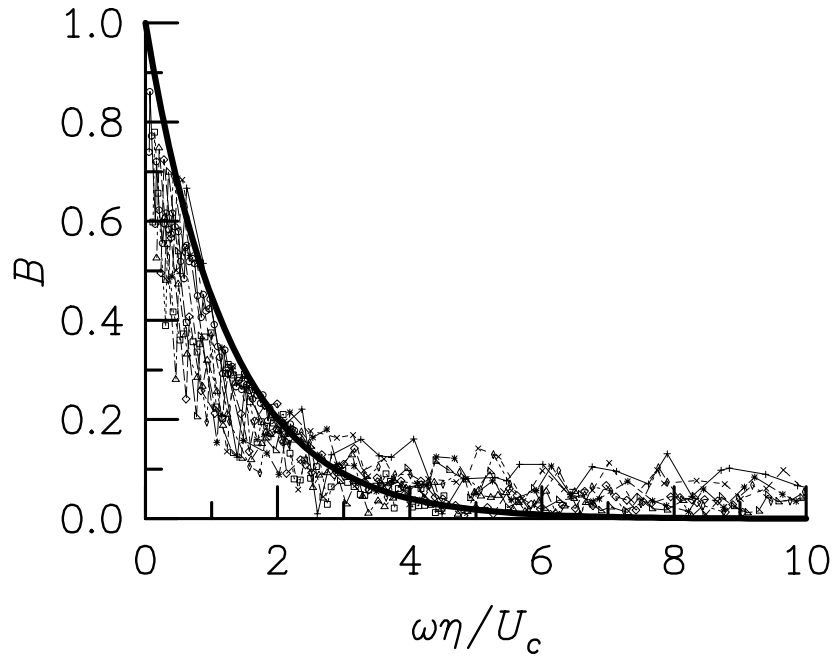


(a) High resolution.

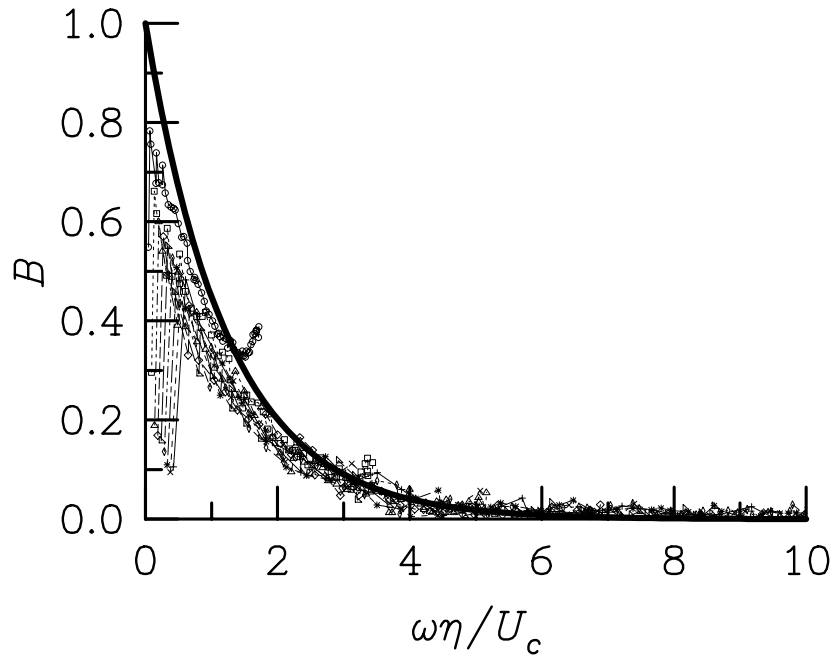


(b) Low resolution.

Figure 13. Convection velocity as function of frequency for different separation distances. Solid line represents extrapolation to $\xi/\delta^* = 0.0$. \circ $\xi/\delta^* = 0.47$; \square $\xi/\delta^* = 2.34$; \triangle $\xi/\delta^* = 4.21$; \diamond $\xi/\delta^* = 6.08$; \triangleright $\xi/\delta^* = 7.95$.

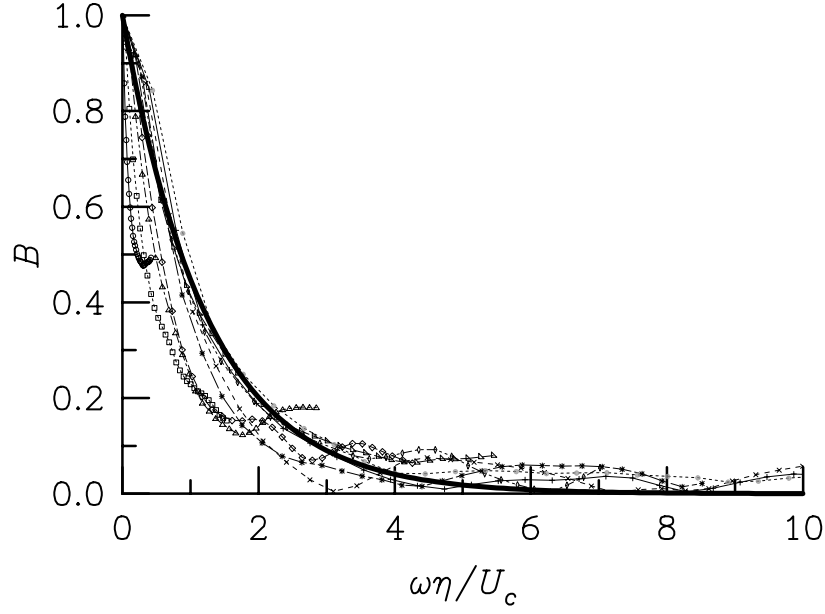


(a) High resolution.

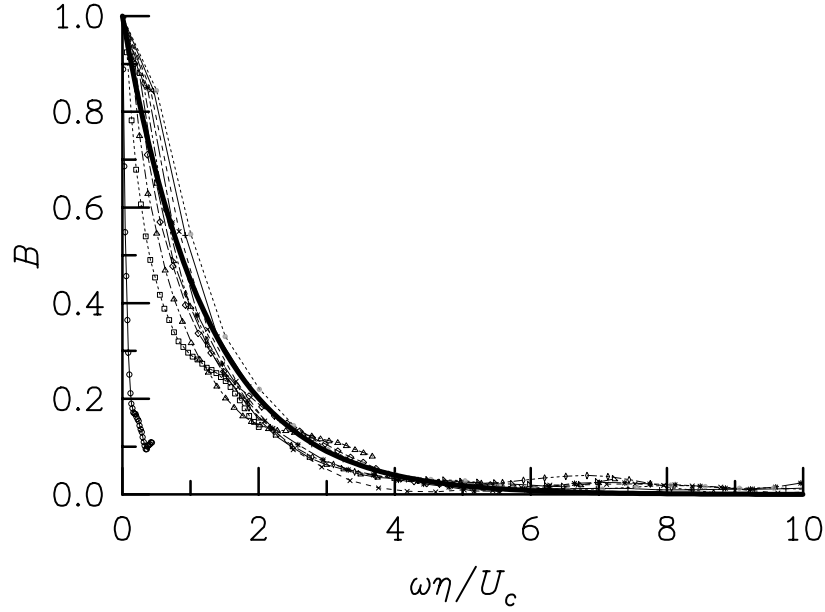


(b) Low resolution.

Figure 14. Spanwise coherence of cross-spectral density. Thick line is $\exp(-0.8|\omega\eta/U_c|)$. Symbols are curves for different separation distances. $\circ \eta/\delta^* = 0.45$; $\square \eta/\delta^* = 0.89$; $\triangle \eta/\delta^* = 1.34$; $\diamond \eta/\delta^* = 1.79$; $\triangleright \eta/\delta^* = 2.23$; $\diamond \eta/\delta^* = 2.68$; $* \eta/\delta^* = 3.12$; $\times \eta/\delta^* = 3.57$; $+ \eta/\delta^* = 4.02$.

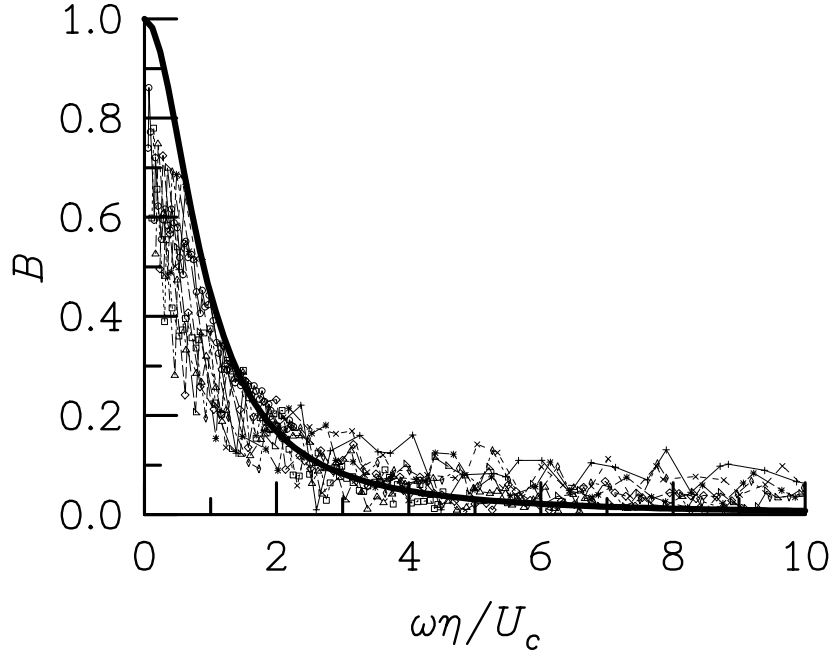


(a) High resolution. $\circ \omega\delta^*/u_\tau = 1.11$; $\square \omega\delta^*/u_\tau = 6.67$; $\triangle \omega\delta^*/u_\tau = 12.23$; $\diamond \omega\delta^*/u_\tau = 17.79$; $\triangleright \omega\delta^*/u_\tau = 23.35$; $\diamond \omega\delta^*/u_\tau = 28.91$; $* \omega\delta^*/u_\tau = 34.47$; $\times \omega\delta^*/u_\tau = 40.03$; $+ \omega\delta^*/u_\tau = 45.59$; $\bullet \omega\delta^*/u_\tau = 51.15$.

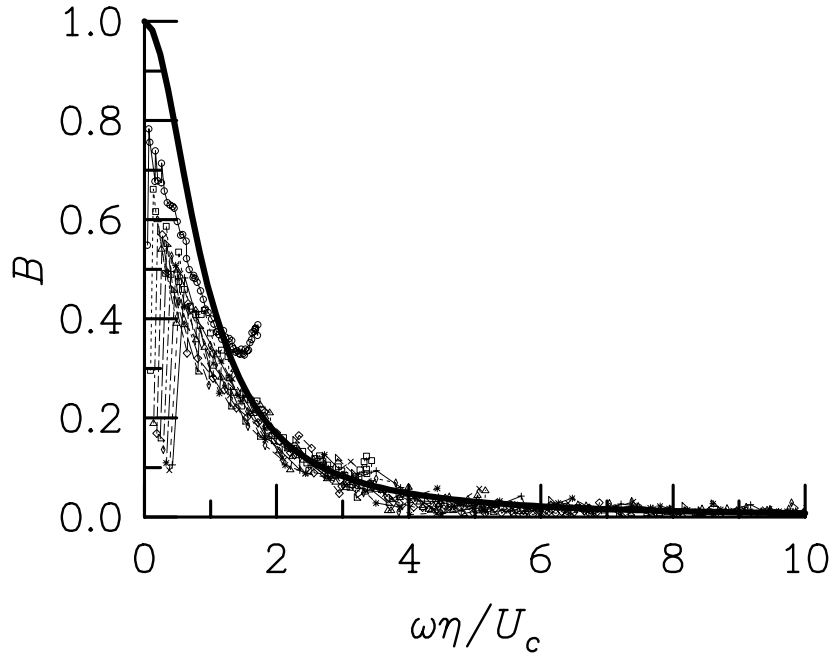


(b) Low resolution. $\circ \omega\delta^*/u_\tau = 1.12$; $\square \omega\delta^*/u_\tau = 6.74$; $\triangle \omega\delta^*/u_\tau = 12.35$; $\diamond \omega\delta^*/u_\tau = 17.97$; $\triangleright \omega\delta^*/u_\tau = 23.58$; $\diamond \omega\delta^*/u_\tau = 29.20$; $* \omega\delta^*/u_\tau = 34.81$; $\times \omega\delta^*/u_\tau = 40.42$; $+ \omega\delta^*/u_\tau = 46.04$; $\bullet \omega\delta^*/u_\tau = 51.65$.

Figure 15. Spanwise coherence of cross-spectral density. Thick line is $\exp(-0.8|\omega\eta/U_c|)$. Symbols are curves for different frequencies.

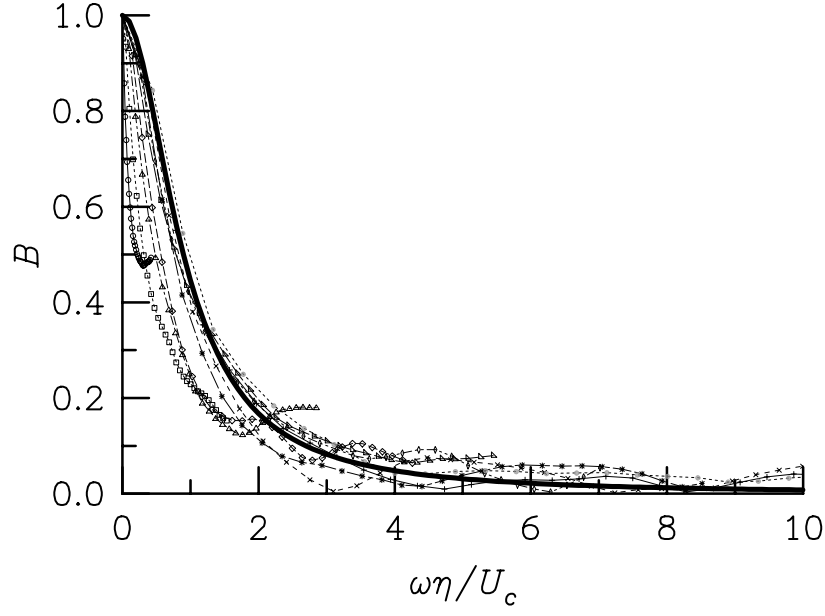


(a) High Resolution.

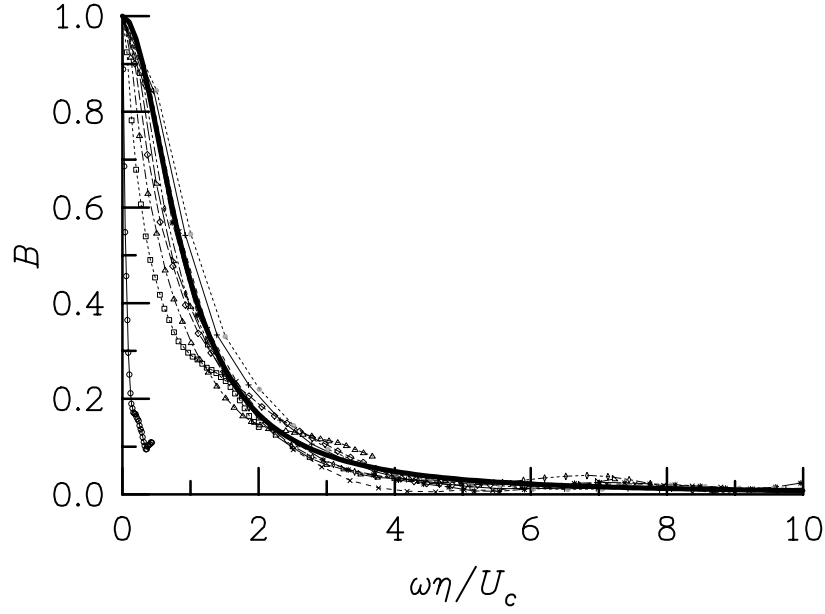


(b) Low resolution.

Figure 16. Spanwise coherence of cross-spectral density. Thick line is $C_s^2/[C_s^2 + (\omega\eta/U_c)^2]$ with $C_s = 0.9$. Symbols are curves for different separation distances. $\circ \eta/\delta^* = 0.45$; $\square \eta/\delta^* = 0.89$; $\triangle \eta/\delta^* = 1.34$; $\diamond \eta/\delta^* = 1.79$; $\triangleright \eta/\delta^* = 2.23$; $\diamond \eta/\delta^* = 2.68$; $* \eta/\delta^* = 3.12$; $\times \eta/\delta^* = 3.57$; $+ \eta/\delta^* = 4.02$.



(a) High resolution. $\circ \omega\delta^*/u_\tau = 1.11$; $\square \omega\delta^*/u_\tau = 6.67$; $\triangle \omega\delta^*/u_\tau = 12.23$; $\diamond \omega\delta^*/u_\tau = 17.79$; $\triangleright \omega\delta^*/u_\tau = 23.35$; $\diamond \omega\delta^*/u_\tau = 28.91$; $* \omega\delta^*/u_\tau = 34.47$; $\times \omega\delta^*/u_\tau = 40.03$; $+ \omega\delta^*/u_\tau = 45.59$; $\bullet \omega\delta^*/u_\tau = 51.15$.



(b) Low resolution. $\circ \omega\delta^*/u_\tau = 1.12$; $\square \omega\delta^*/u_\tau = 6.74$; $\triangle \omega\delta^*/u_\tau = 12.35$; $\diamond \omega\delta^*/u_\tau = 17.97$; $\triangleright \omega\delta^*/u_\tau = 23.58$; $\diamond \omega\delta^*/u_\tau = 29.20$; $* \omega\delta^*/u_\tau = 34.81$; $\times \omega\delta^*/u_\tau = 40.42$; $+ \omega\delta^*/u_\tau = 46.04$; $\bullet \omega\delta^*/u_\tau = 51.65$.

Figure 17. Spanwise coherence of cross-spectral density. Thick line is $C_s^2/[C_s^2 + (\omega\eta/U_c)^2]$ with $C_s = 0.9$. Symbols are curves for different frequencies.